LETTERS

TCR–peptide–MHC interactions *in situ* show accelerated kinetics and increased affinity

Johannes B. Huppa[1], Markus Axmann[3], Manuel A. Mörtelmaier[1,3]†, Björn F. Lillemeier[1]†, Evan W. Newell[1], Mario Brameshuber[3], Lawrence O. Klein[1], Gerhard J. Schütz[3] & Mark M. Davis[1,2]

The recognition of foreign antigens by T lymphocytes is essential to most adaptive immune responses. It is driven by specific T-cell antigen receptors (TCRs) binding to antigenic peptide–major histocompatibility complex (pMHC) molecules on other cells[1]. If productive, these interactions promote the formation of an immunological synapse[2,3]. Here we show that synaptic TCR–pMHC binding dynamics differ significantly from TCR–pMHC binding in solution. We used single-molecule microscopy and fluorescence resonance energy transfer (FRET) between fluorescently tagged TCRs and their cognate pMHC ligands to measure the kinetics of TCR–pMHC binding *in situ*. When compared with solution measurements, the dissociation of this complex was increased significantly (4–12-fold). Disruption of actin polymers reversed this effect, indicating that cytoskeletal dynamics destabilize this interaction directly or indirectly. Nevertheless, TCR affinity for pMHC was significantly elevated as the result of a large (about 100-fold) increase in the association rate, a likely consequence of complementary molecular orientation and clustering. In helper T cells, the CD4 molecule has been proposed to bind cooperatively with the TCR to the same pMHC complex. However, CD4 blockade had no effect on the synaptic TCR affinity, nor did it destabilize TCR–pMHC complexes, indicating that the TCR binds pMHC independently of CD4.

Surface plasmon resonance (SPR) and microcalorimetry experiments with engineered soluble proteins generally show weak TCR–pMHC binding, with affinities (K_d values) in the range 1–100 μM, $t_{1/2}$ values on the order of seconds, and association rates usually ranging from 1,000 to 10,000 $M^{-1}\,s^{-1}$ (refs 4–6). Nevertheless, T cells are highly specific and sensitive for antigen, able to detect even a single antigenic pMHC complex among structurally similar yet non-stimulatory pMHCs[7,8]. However, although this is useful for comparative purposes, these measurements do not account for the many constraints and special features of the synaptic environment and might not reflect what occurs *in situ*. In particular, the restricted intercellular volume should greatly accelerate the association rate and enhance serial engagement[9–11]. Favourable molecular alignment of TCR and MHC, as well as any molecular pre-clustering, could also drastically affect binding[12–14]. Although the volume effect can be approximated, the influence of the others is essentially unknown. We have therefore devised a method to measure synaptic TCR binding to pMHC directly, using single-molecule microscopy and FRET between a donor fluorophore on the TCR and an acceptor fluorophore on the peptide bound to a MHC molecule.

We used T-cell blasts from two different TCR transgenic T-cell lines, 2B4 and 5c.c7, which are specific for the same moth cytochrome *c* peptide (MCC 88–103) bound to the class II MHC molecule IE^k. To permit the use of highly sensitive and rapid total internal reflection (TIRF) microscopy, we used a modified planar lipid bilayer system as a surrogate antigen-presenting cell surface, presenting IE^k complexes, ICAM-1 adhesion molecules and B7-1 co-stimulatory polypeptides (see Methods).

Structural analysis of an Fab fragment derived from the monoclonal anti-TCR-β antibody H57 complexed with the Cβ region of a TCR indicated that portions of its binding site might be close enough to the carboxy terminus of a peptide bound to a MHC (about 41 Å)[15,16] to allow FRET *in situ* to measure TCR binding. We therefore constructed a single-chain variable fragment (scFv) of this antibody with mutations that could be labelled at three different sites (J1, J2 and J3). Their location and proximity to the C terminus of a peptide bound to the IE^k molecule are shown (Fig. 1a).

On addition of the Cy3-labelled J1 reagent to 5c.c7 transgenic T cells on bilayers containing IE^k/MCC(C)-Cy5, we observed the rapid onset of a FRET signal, which was corrected for donor bleed-through and acceptor cross-excitation (see Methods). Consistent with the FRET results was the observation that this signal disappeared immediately after ablation of the FRET acceptor, together with an increase in donor intensity (Fig. 1b). Reversing the labels produced comparable results (Fig. 1b and Supplementary Fig. 1a). The average synaptic FRET yield (as measured by donor recovery after acceptor bleaching; see Methods) was 10–12% for the agonists IE^k/MCC(C)-Cy5 and IE^k/K5(C)-Cy5 (Fig. 1c). FRET was highly dependent on the ligand: no synaptic FRET was observed between the J1-Cy3-labelled TCR and the null ligands IE^k/β_2M(C)-Cy5 or IE^k/MCC null(C)-Cy5, even in the presence of unlabelled agonists (IE^k/MCC) to ensure T-cell activation (Fig. 1b, c). The FRET strength correlated with both the density of labelled IE^k/peptide(C)-Cy5 and the ligand potency (Supplementary Fig. 1b). No FRET was detectable when T cells were labelled with a Cy3-conjugated anti-CD4 Fab (GK1.5), further validating signal specificity (Fig. 1c).

To assess potential bystander FRET between TCR–pMHC complex-bound J1-Cy3 and neighbouring pMHCs, we tested the J1, J2 and J3 probes in conjunction with the agonist ligand IE^k/K5 labelled at either the C or N terminus of the peptide. These combinations gave rise to six inter-dye distances ranging from about 41 Å to about 100 Å. Average synaptic FRET depended strictly on the distance between the dye pair, as expected, given that yields of FRET decline inversely with the sixth power of the distance (Fig. 1d). Hence, this assay is specific for individual TCR–ligand interactions, and bystander effects are negligible.

We also used single-molecule FRET (smFRET) microscopy to derive dissociation rates. After correcting for donor bleed-through and acceptor cross-excitation, we identified smFRET events as those that both co-localized with single acceptor molecules and also

[1]Department of Microbiology and Immunology, Stanford School of Medicine, and [2]Howard Hughes Medical Institute, Beckman Center B221, 279 Campus Drive, Stanford, California 94305-5323, USA. [3]Institut für Biophysik, Johannes Kepler-Universität, Altenbergerstrasse 69, A-4040 Linz, Austria. †Present addresses: Agilent Technologies Austria, Mooslackengasse 17, 1190 Wien, Austria (M.A.M.); Nomis Center for Immunobiology and Microbial Pathogenesis, Waitt Advanced Biophotonics Center, The Salk Institute, 10010 North Torrey Pines Road, La Jolla, California 92037, USA (B.F.L.).

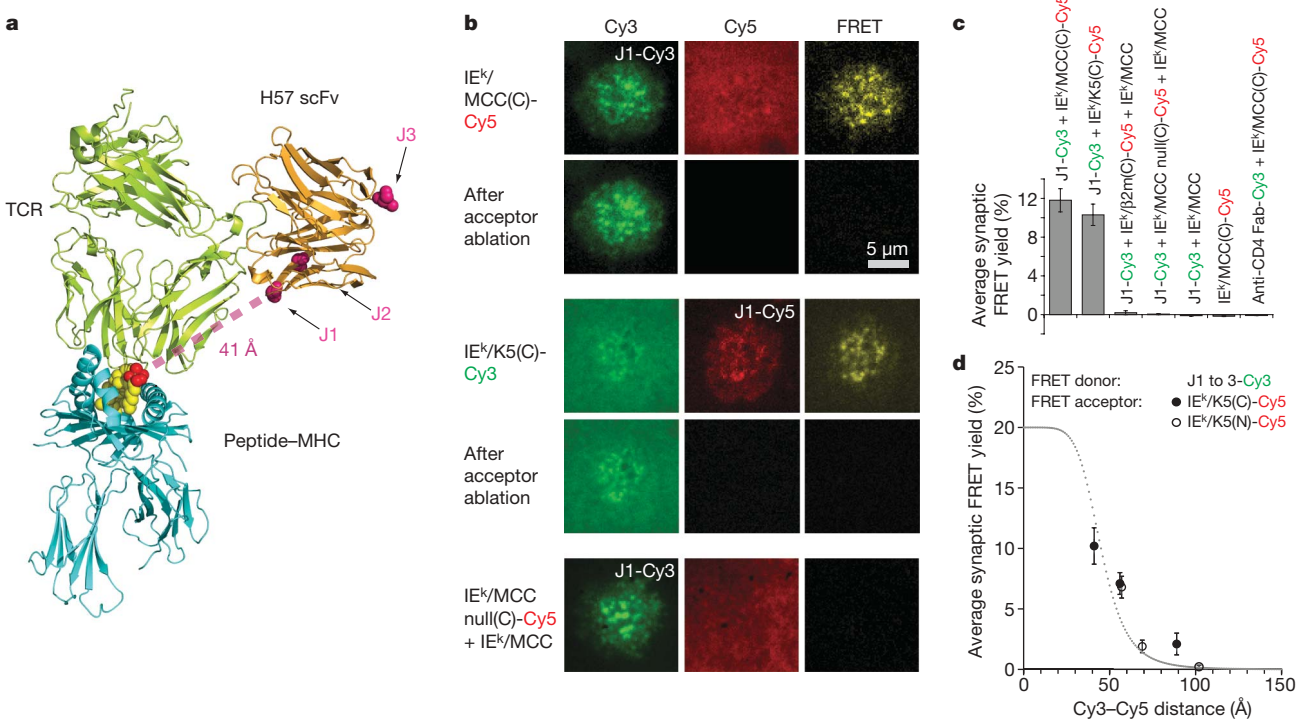

Figure 1 | FRET as a sensor for TCR–ligand interactions. a, Composite model based on the TCR–pMHC and TCR–H57 Fab structures. J1–J3 indicate dye attachment sites. **b**, Cy3, Cy5 and corrected FRET channels before and after acceptor bleaching at 24 °C. Scale bar, 5 μm. **c**, **d**, FRET yields determined through donor recovery after receptor bleaching. Error bars represent s.e.m. ($n \geq 40$; temperature 24 °C, $\rho(IE^k/\text{peptide-Cy5}) = 120\ \mu m^{-2}$). **c**, Ligand specificity of the FRET yield. **d**, Relationship between Cy3(FRET donor)–Cy5(FRET acceptor) distance and FRET yield. Cy3–Cy5 distances were estimated from **a**, excluding the length of the linker and dye. The dotted line in **d** equals theoretical synaptic FRET yield ($R_0 = 4.6$ nm) with a maximum (roughly 20%) predicted from experiments shown in Supplementary Fig. 23b.

appeared and disappeared in a single step—a hallmark of single-molecule behaviour (Fig. 2a and Supplementary Figs 2–7). Furthermore, the appearance of these events was specific to label and ligand: other label combinations, including J3-Cy3 or IE^k/MCC-null(C)-Cy5, did not produce such events (data not shown). Reversing the label proportion by employing IE^k/MCC(C)-Cy5 in high abundance and J1-Cy3 in low abundance also led to smFRET events (Supplementary Figs 8–10). By monitoring the duration of these FRET signals during synapse formation and correcting for photobleaching (see Methods), we determined the dissociation rates for both the 5c.c7 TCR and the 2B4 TCR with IE^k/MCC at 37 °C and for 5c.c7 with the weak agonist T102S (Fig. 2b, Table 1 and Supplementary Fig. 1c). These data followed single-exponential decay kinetics, which is consistent with a simple dissociation of the TCR–pMHC complex. Unexpectedly, the $t_{1/2}$ values for these interactions were much shorter than those measured *in vitro* by SPR, especially for the 5c.c7 TCR (Fig. 2c). Across a temperature range we found that synaptic $t_{1/2}$ values were consistently 3–12-fold shorter than those measured *in vitro*, especially at higher temperatures. Recently, a continual 'flow' of actin in synapse-forming T cells from the periphery to near the centre of the synapse has been shown[17]. To determine whether this could be the cause of the shorter $t_{1/2}$ values, we employed the actin-depolymerizing drugs cytochalasin D and latrunculin A. These treatments greatly prolonged synaptic TCR–pMHC interactions, indicating that actin dynamics destabilizes TCR–ligand interactions either directly or indirectly (Fig. 2d). Under these conditions the $t_{1/2}$ is almost identical to that measured by SPR (4.23 s or 4.78 s *in situ*, versus 3.5 s *in vitro*) with the synaptic $t_{1/2}$ being slightly greater; this is expected because diffusion is more limited in that environment.

To estimate the affinity, we calculated the concentrations of the reactants and their products by first determining the local density (ρ) of total TCRs, pMHCs and TCR–pMHC complexes in a representative synapse. This was done on the basis of the average intensities of single-molecule fluorescence (Supplementary Fig. 21). To ensure a TCR labelling efficiency of at least 95%, we analysed synapses for 2.5 min or less at 24 °C (where the $t_{1/2}$ for scFv is about 50 min). With this image information (Fig. 3) we calculated the average local effective two-dimensional K_a (2D K_a) ($K_a = 1/K_d$) and, using the k_{off} determined above, the k_{on} ($k_{on} = K_a k_{off}$; Fig. 3a; see Methods). Hotspots of TCR binding are apparent, indicating that both local cellular parameters and the intrinsic chemistry of the interactions influence binding behaviour.

We also measured the affinities within individual TCR microclusters. To conduct our studies at higher temperatures we quantified the TCR occupancy of TCRs in individual TCR microclusters through their individual FRET yield (as measured by acceptor bleaching), which is independent of the degree of TCR labelling. This and a knowledge of the pMHC density in the bilayer allowed us to calculate the effective 2D K_d values (see Methods). The 2D K_d values for individual TCR microclusters varied significantly (about 250-fold), most probably because of locally active cellular parameters (Fig. 3b). We give the median *in situ* K_d values for comparison in Table 1.

To derive the effective synaptic three-dimensional K_d (3D K_d) of the interactions taking place within a TCR microcluster for comparison with the corresponding value measured by SPR, we converted the area for which binding was observed into the volume of the intermembrane space. To calculate the concentration we divided the density by the distance of 13.4 nm between the opposed membranes. This width is also the approximate maximum distance at which a TCR and pMHC could interact if fully extended and perpendicular to the plane of their respective membranes[18]. It is also consistent with electron microscopic analyses of synapses[19]. For the interaction between 5c.c7 TCR and IE^k/MCC at 37 °C (at a density of 30 IE^k/MCC(C)-Cy5 μm^{-2}), this resulted in a median K_d of 4.8 μM, which is about 8.3-fold lower than the value determined *in vitro*, despite the about 12-fold accelerated decay rate that we observed *in situ*. Assuming steady-state conditions, we calculated a median synaptic k_{on} of $1.38 \times 10^6\ M^{-1}\ s^{-1}$, an almost 100-fold increase compared with the SPR value at 37 °C (Fig. 3c and

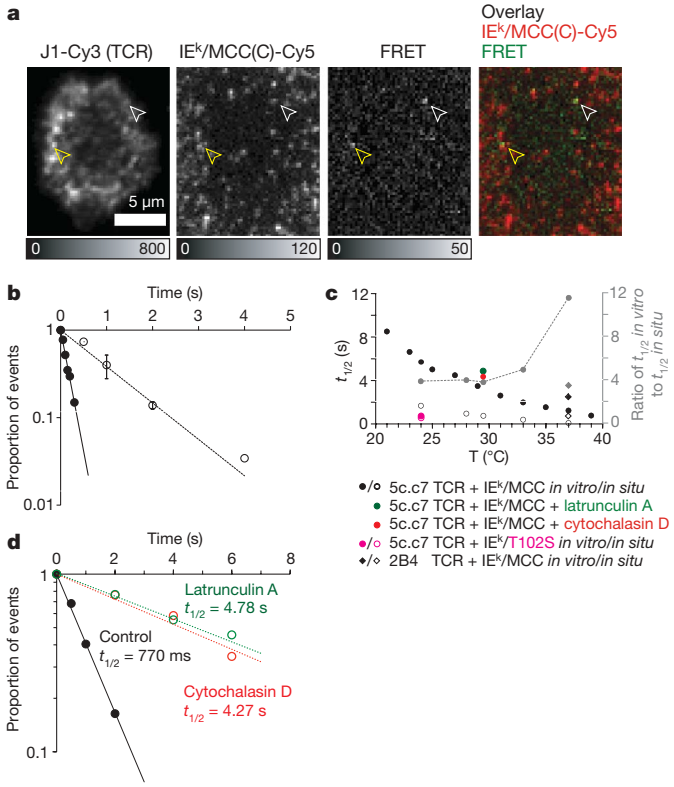

Figure 2 | Synaptic off-rates measured through smFRET. a, High-abundance FRET donor J1-Cy3, single molecule IE^k/MCC(C)-Cy5 (acceptor), smFRET channel and overlaid single-molecule channels are indicated. The white arrows indicate a single FRET event co-localizing with a single FRET acceptor, and the yellow arrows a candidate event co-localizing with several FRET acceptors. The intensity bars show counts per pixel. Scale bar, 5 μm. **b**, Decay plot of interactions between synaptic TCR(J1-Cy3) and IE^k/MCC(C)-Cy5 at 37 °C. Open circles, 2B4 TCR ($t_{1/2}$ = 723 ms); filled circles, 5c.c7 TCR ($t_{1/2}$ = 109 ms). Error bars represent the standard deviation of the mean of the values as determined with different acquisition delays (for example 500, 1,000 and 2000 ms). **c**, Temperature spectrum of measured $t_{1/2}$ values of interactions between 5c.c7 and IE^k/MCC and between 2B4 TCR and IE^k/MCC (*in vitro*:*in situ* $t_{1/2}$ ratios are shown in grey). **d**, Interactions between 5c.c7 TCR and IE^k/MCC at 29.5 °C are prolonged on disruption of cortical actin through cytochalasin D and latrunculin A.

Table 1). We also determined the dependence of the TCR affinity on the density of ligands presented on the bilayer at 37 °C. Although constant at low and moderate pMHC densities, the median synaptic affinity decreased at ligand densities approaching that of the TCR, suggesting that some TCRs are refractory to binding (Fig. 3d and Table 1).

Synaptic binding properties also correlated with signalling potency: TCR binding was strongest for the agonist IE^K/MCC, followed by the weak agonist IE^K/T102S and the antagonists IE^K/T102G and IE^K/K99R (Fig. 3e). IE^K/T102S showed a single-exponential decay curve (Supplementary Fig. 1c) with a $t_{1/2}$ 2.4-fold lower (0.7 s) than that of IE^k/MCC. This difference is less than sevenfold, as seen with the equivalent SPR measurements (Table 1) and probably reflects the impaired signalling activity of this ligand (see below).

Of special interest with regard to helper T-cell recognition is the role of the CD4 co-receptor, which binds to a non-polymorphic region within MHC class II with a barely measurable affinity (250 μM or more)[20], yet has a main role in T-cell sensitivity[7]. A widely held view is that, to initiate signalling, simultaneous binding of TCR and CD4 to the same pMHC ligand directly recruits the TCR-proximal kinase p56^{lck} to the TCR through the association of p56^{lck} with CD4 (refs 21, 22). Other models suggest that CD4 is associated with the TCR but does not bind the same MHC class II as its associated TCR[7,22]. To distinguish between these two models, we first compared the average synaptic TCR–pMHC FRET yield in the absence and presence of CD4 blockade, because the FRET yield is related to the average synaptic TCR–pMHC affinity (Supplementary Fig. 12). CD4 blockade had little or no effect on the synaptic affinity between TCR and pMHC, both early and later in synapse formation. smFRET analysis revealed that CD4 blockade slightly stabilized interactions (Fig. 4a). An explanation could be that CD4 blockade attenuates T-cell signalling (Fig. 4b, c). This could dampen cellular motility, which destabilizes TCR–pMHC interactions. Thus we repeated CD4 blocking in the presence of pp2 (a p56^{lck} inhibitor) or cytochalasin D, which completely abrogated the CD4-mediated difference in the binding off-rate (Fig. 4d, e). Thus, the increased TCR–pMHC stability is due to signalling effects. Taken together, these results show that TCRs bind to ligands independently of CD4 and are not, as previously proposed, joined to CD4 molecules as a physical unit. TCR and CD4 could nevertheless still bind the same agonist pMHC simultaneously[21], because independent and simultaneous binding events are not mutually exclusive, whether in solution or within the synapse. Because CD4 engagement boosts T-cell activation and sensitivity throughout synapse formation (Fig. 4b, c, and Supplementary Fig. 13), the function of CD4 seems likely to be that of signal reinforcement through its intracellular association with p56^{lck} once a TCR has engaged a viable ligand[21].

Our data offer new insights into both how TCRs discriminate between different peptide-MHC ligands and also the unique challenges of finding and deriving the maximal signalling potential from even very rare agonists. In view of our data, the phosphorylation of TCR-associated CD3 signalling chains—that is, the first step in response

Table 1 | Summary of measured binding constants

Ligand	Temperature (°C)	Density* (molecules μm^{-2})	Median† *in situ* 3D K_d (μM)	*In vitro*‡ K_d (μM)	*In situ* $t_{1/2}$ (s) [k_{off} (s^{-1})]	*In vitro*‡ $t_{1/2}$ (s) [k_{off} (s^{-1})]	Median† *in situ* 3D k_{on} (s^{-1} M^{-1})	*In vitro*‡ k_{on} (s^{-1} M^{-1})
IE^k/MCC	24.0	30	4.26	22.9	1.68 [0.41]	5.77 [0.120]	9.75×10^4	3.31×10^3
IE^k/MCC	28.0	30	4.33	24.7	1.25 [0.55]	4.0 [0.173]	1.26×10^5	5.49×10^3
IE^k/MCC, CD4 block	28.0	30			1.63 [0.43]			
IE^k/MCC, pp2	28.0	30			1.57 [0.44]			
IE^k/MCC	29.5	30			0.77 [0.90]			
IE^k/MCC, Cyt D	29.5	30			4.23 [0.163]			
IE^k/MCC, Lat A	29.5	30			4.78 [0.144]			
IE^k/MCC	33.0	30	4.02	27.7	0.405 [1.7]	2.28 [0.305]	4.22×10^5	1.12×10^4
IE^k/MCC	37.0	30	4.8	39.8	0.109 [6.36]	1.24 [0.559]	1.38×10^6	1.40×10^4
IE^k/MCC	37.0	6	4.16		0.138 [5]		1.20×10^6	
IE^k/MCC	37.0	150	8.67		0.111 [6.25]		7.20×10^5	
IE^k/T102S	24.0	30			0.7 [1.02]	0.82 [0.838]		
IE^k/T102S	24.0	139	18.2	206			5.59×10^4	4.05×10^3
IE^k/T102S, Lat A	24.0	30			0.99 [0.7]			
IE^k/T102G	24.0	175	42.6					
IE^k/K99R	24.0	175	208					

Cyt D, cytochalasin D; Lat A, latrunculin A.
* Where applicable.
† Values measured in individual TCR microclusters.
‡ Values obtained by SPR.

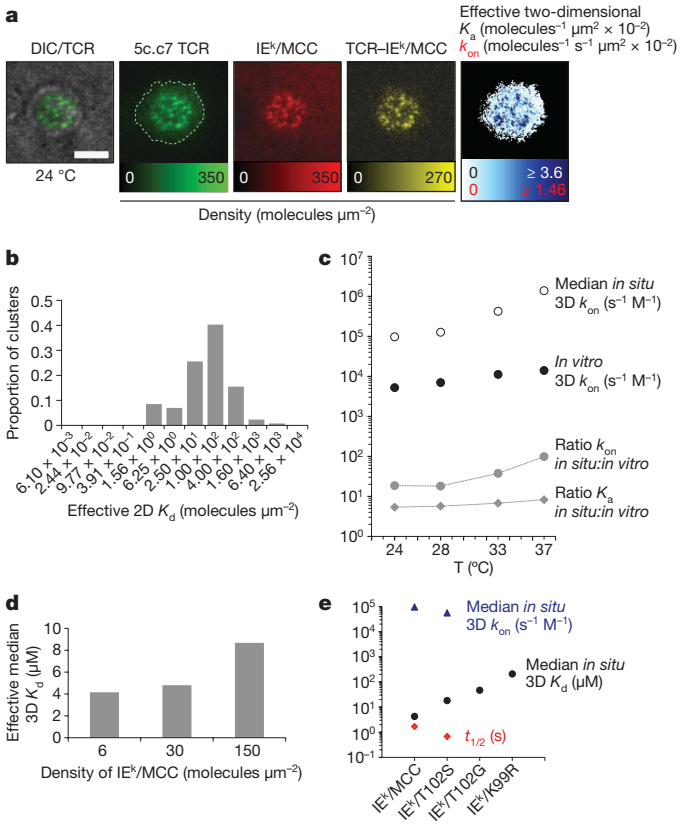

Figure 3 | Quantitative image analysis yields effective synaptic 2D K_d, 2D K_a and 2D k_{on}. **a**, Synaptic density plots of TCR, IE^k/MCC and TCR–IE^k/MCC result in a 2D K_a plot (white print) and 2D k_{on} plot (red print). Dashed line, synapse boundary. Scale bar, 5 μm. **b**, 2D K_d distribution was measured for 5c.c7 TCR–IE^k/MCC microclusters at 37 °C. Values on the *x* axis show the upper interval boundary. The median value is 38.8. **c**, 3D k_{on} values were determined in 5c.c7 TCR–IE^k/MCC microclusters and by SPR. *In situ:in vitro* k_{on} ratios and *in vitro:in situ* K_d ratios are shown. **d**, 3D K_d values are shown for 5c.c7 TCR microclusters interacting at 37 °C with bilayers containing IE^k/MCC(C)-Cy5 at the indicated densities. **e**, 3D K_d, 3D k_{on} and $t_{1/2}$ values were measured at 24 °C in 5c.c7 TCR microclusters in contact with the indicated ligands.

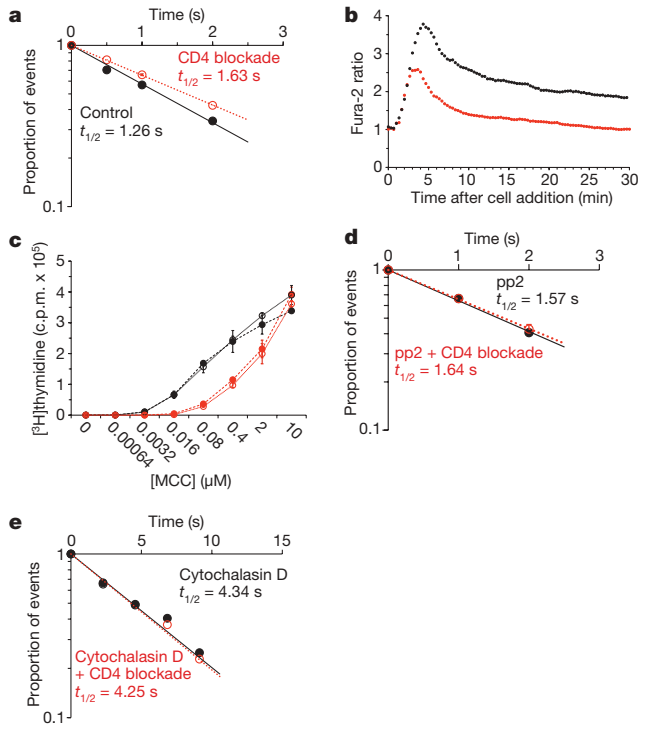

Figure 4 | Effect of CD4 on TCR signalling and ligand binding. **a**, Decay of interactions between synaptic 5c.c7 TCR and IE^k/MCC at 28 °C in the absence (black) and presence (red) of CD4 antibody blockade. **b**, Calcium signalling at 28 °C in the absence (black) and presence (red) of CD4 antibody blockade. **c**, T-cell proliferation (as measured by [^{3}H]thymidine incorporation into naive T cells in response to varying doses of antigenic peptide) in the absence (black) and presence (red) of CD4 antibody blockade. Open symbols, with H57 scFv; filled symbols, without H57 scFv. Error bars represent the standard deviation of the mean for data sets measured in triplicate. **d**, CD4 blockade did not affect the synaptic $t_{1/2}$ of the 5c.c7 TCR–IE^k/MCC complex at 28 °C after inhibition of the activity of p56^{lck} with pp2. **e**, CD4 blockade did not affect the synaptic $t_{1/2}$ of the 5c.c7 TCR–IE^k/MCC complex at 29.5 °C after disruption of the actin cortex with cytochalasin D.

to receptor engagement—is certain to result from frequent yet short-lived binding events. This means that, for the 5c.c7 TCR with its $t_{1/2}$ of about 100 ms, there could be roughly 3,000 separate receptor–ligand interactions in 1 min if ten ligands were engaged simultaneously in a synapse *in situ*, as is required for maximal calcium activation and stable synapse formation[7]. If the ligands were fully occupied and each interaction gave rise to a single signalling event, there would be a significant rate of TCR signal transduction, equivalent to triggering about 10% of the TCRs in the cell.

How could rare pMHCs be kept occupied by TCRs, which are relatively sparse and have such unstable interactions? The explanation may lie in 'protein islands', distinct 10–200-nm membrane microdomains highly enriched for particular membrane proteins[12,13]. We find that clusters of TCRs are expressed on a subset of these islands, as also suggested by others[14]. Such TCR islands could efficiently 'scan' the surface of an adjacent cell and provide a high local density of TCRs surrounding a ligand to keep it continually engaged to generate the maximum possible signal. This is also consistent with cholesterol-depletion experiments in which TCR binding was no longer punctate: binding was decreased fivefold at higher and moderate pMHC densities and was no longer detectable at low densities (Supplementary Fig. 14). Receptor and ligand aggregation might also be facilitated by weak lateral interactions, substrate topography, membrane rigidities and line tension[23,24].

Differences in kinetic binding parameters could be substantially enhanced in a synaptic environment. Pre-oriented binding partners, molecular clustering and active T-cell scanning mechanisms would raise the frequency of otherwise rare molecular encounters. In contrast, interactions with a low $\Delta\Delta G$ might be even less stable as a result of cellular forces acting against them. In particular, we found that the 5c.c7-TCR of 'average' affinity was more severely destabilized (about 12-fold) than a higher-affinity 2B4-TCR (fourfold). This suggests that this unexpected activity in the synapse could help select for better-quality ligands and against weaker ones.

We have used a new imaging strategy to measure the binding of the TCR to its peptide–MHC ligand. Within an immunological synapse this shows that this very specialized but ubiquitous environment enhances the ability of otherwise very weak and rare ligands to drive important biological effects. With antibody pairs, for example, this FRET strategy could be used to characterize other molecular interactions as well. It seems likely that at least some of the binding characteristics found here will be shared with other cell-surface receptors on other cells, because molecules of this type generally have affinities and dissociation rates in the same range as TCRs[10,11,18].

METHODS SUMMARY

We take advantage of FRET to measure *in situ* the synaptic interactions between cell-bound TCRs and their cognate ligands, pMHC, embedded in a planar lipid bilayer. We engineered a site-specifically labelled TCR-reactive scFv to tag cell-surface-located TCRs. When the TCR is bound to its ligand, its associated scFv brings its label (FRET donor) close enough to the FRET acceptor dye attached to

the MHC-embedded peptide to give rise to a FRET signal. We recorded smFRET to measure the $t_{1/2}$ values of synaptic TCR–pMHC interactions. We combined smFRET and bulk FRET measurements to determine synaptic K_d values and k_{on} values. We applied antibody-mediated blockade of CD4 to assess its contribution to TCR–pMHC binding.

Full Methods and any associated references are available in the online version of the paper at www.nature.com/nature.

Received 24 February; accepted 7 December 2009.

1. Davis, M. M. *et al.* T cells as a self-referential, sensory organ. *Annu. Rev. Immunol.* **25,** 681–695 (2007).
2. Grakoui, A. *et al.* The immunological synapse: a molecular machine controlling T cell activation. *Science* **285,** 221–227 (1999).
3. Monks, C. R., Freiberg, B. A., Kupfer, H., Sciaky, N. & Kupfer, A. Three-dimensional segregation of supramolecular activation clusters in T cells. *Nature* **395,** 82–86 (1998).
4. Corr, M. *et al.* T cell receptor-MHC class I peptide interactions: affinity, kinetics, and specificity. *Science* **265,** 946–949 (1994).
5. Matsui, K., Boniface, J. J., Steffner, P., Reay, P. A. & Davis, M. M. Kinetics of T-cell receptor binding to peptide/I-Ek complexes: correlation of the dissociation rate with T-cell responsiveness. *Proc. Natl Acad. Sci. USA* **91,** 12862–12866 (1994).
6. Krogsgaard, M. *et al.* Evidence that structural rearrangements and/or flexibility during TCR binding can contribute to T cell activation. *Mol. Cell* **12,** 1367–1378 (2003).
7. Irvine, D. J., Purbhoo, M. A., Krogsgaard, M. & Davis, M. M. Direct observation of ligand recognition by T cells. *Nature* **419,** 845–849 (2002).
8. Sykulev, Y., Joo, M., Vturina, I., Tsomides, T. J. & Eisen, H. N. Evidence that a single peptide-MHC complex on a target cell can elicit a cytolytic T cell response. *Immunity* **4,** 565–571 (1996).
9. Bell, G. I. Models for the specific adhesion of cells to cells. *Science* **200,** 618–627 (1978).
10. Dustin, M. L., Ferguson, L. M., Chan, P. Y., Springer, T. A. & Golan, D. E. Visualization of CD2 interaction with LFA-3 and determination of the two-dimensional dissociation constant for adhesion receptors in a contact area. *J. Cell Biol.* **132,** 465–474 (1996).
11. Zhu, D. M., Dustin, M. L., Cairo, C. W. & Golan, D. E. Analysis of two-dimensional dissociation constant of laterally mobile cell adhesion molecules. *Biophys. J.* **92,** 1022–1034 (2007).
12. Lillemeier, B. F. *et al.* TCR and LAT occur in separate membrane domains and concatenate during activation. *Nature Immunol.* **11,** 90–96 (2010).
13. Lillemeier, B. F., Pfeiffer, J. R., Surviladze, Z., Wilson, B. S. & Davis, M. M. Plasma membrane-associated proteins are clustered into islands attached to the cytoskeleton. *Proc. Natl Acad. Sci. USA* **103,** 18992–18997 (2006).
14. Schamel, W. W. *et al.* Coexistence of multivalent and monovalent TCRs explains high sensitivity and wide range of response. *J. Exp. Med.* **202,** 493–503 (2005).
15. Garcia, K. C. *et al.* Structural basis of plasticity in T cell receptor recognition of a self peptide-MHC antigen. *Science* **279,** 1166–1172 (1998).
16. Wang, J. *et al.* Atomic structure of an αβ T cell receptor (TCR) heterodimer in complex with an anti-TCR Fab fragment derived from a mitogenic antibody. *EMBO J.* **17,** 10–26 (1998).
17. Kaizuka, Y., Douglass, A. D., Varma, R., Dustin, M. L. & Vale, R. D. Mechanisms for segregating T cell receptor and adhesion molecules during immunological synapse formation in Jurkat T cells. *Proc. Natl Acad. Sci. USA* **104,** 20296–20301 (2007).
18. van der Merwe, P. A., McNamee, P. N., Davies, E. A., Barclay, A. N. & Davis, S. J. Topology of the CD2–CD48 cell-adhesion molecule complex: implications for antigen recognition by T cells. *Curr. Biol.* **5,** 74–84 (1995).
19. Choudhuri, K., Wiseman, D., Brown, M. H., Gould, K. & van der Merwe, P. A. T-cell receptor triggering is critically dependent on the dimensions of its peptide-MHC ligand. *Nature* **436,** 578–582 (2005).
20. Xiong, Y., Kern, P., Chang, H. & Reinherz, E. T cell receptor binding to a pMHCII ligand is kinetically distinct from and independent of CD4. *J. Biol. Chem.* **276,** 5659–5667 (2001).
21. Li, Q. J. *et al.* CD4 enhances T cell sensitivity to antigen by coordinating Lck accumulation at the immunological synapse. *Nature Immunol.* **5,** 791–799 (2004).
22. Krogsgaard, M. *et al.* Agonist/endogenous peptide-MHC heterodimers drive T cell activation and sensitivity. *Nature* **434,** 238–243 (2005).
23. Fricke, G. M. & Thomas, J. L. Receptor aggregation by intermembrane interactions: a Monte Carlo study. *Biophys. Chem.* **119,** 205–211 (2006).
24. Weikl, T. R. & Lipowsky, R. Pattern formation during T-cell adhesion. *Biophys. J.* **87,** 3665–3678 (2004).

Supplementary Information is linked to the online version of the paper at www.nature.com/nature.

Acknowledgements We thank F. E. Tynan, A. K. Chakraborty and S. R. Quake for helpful discussions, and P. P. J. Ebert for help with the flow cytometry experiments. This work was supported by grants from the National Institutes of Health (RO1 AI52211) and the Howard Hughes Medical Institute to M.M.D. J.B.H. is partly supported by the Immunology Frontier Research Center (iFREC) consortium, M.A.M. received a postdoctoral fellowship from the Wilhelm Macke Stiftung, and E.W.N. from the American Cancer Society's Steven Stanley and Edward Albert Bielfelt Fund. L.O.K. is supported by a National Science Foundation predoctoral fellowship. M.A., M.B. and G.J.S. received grants from the Austrian Science Fund (project Y250-B10) and the GEN-AU project of the Austrian Ministry for Science and Research.

Author Contributions J.B.H., G.J.S. and M.M.D. conceived the project. Reagents and experimental systems were designed and tested by J.B.H. unless indicated otherwise. M.A., M.A.M. and G.J.S. provided important expertise in single-molecule microscopy. M.A. conducted all single dye tracing experiments and all smFRET experiments performed in Linz. J.B.H. conducted all bulk FRET experiments and all smFRET experiments at Stanford. J.B.H. and M.A.M. laid the experimental foundation in the initial phase of the project. M.A.M. provided important expertise in setting up the microscope system at Stanford. B.F.L. provided the expression system for ICAM-1 and B7-1. E.W.N. conducted all SPR measurements. M.B. conducted all TOCCSL experiments. L.O.K. and B.F.L. contributed important ideas. J.B.H. and M.M.D. wrote the manuscript.

Author Information Reprints and permissions information is available at www.nature.com/reprints. The authors declare no competing financial interests. Correspondence and requests for materials should be addressed to M.M.D. (mmdavis@stanford.edu).

METHODS

Protein expression and preparation. ICAM-1–His_{12} and B7-1–His_{12} were expressed with a baculovirus system and $IE^k\alpha\beta$ ($2 \times His_6$) in *Drosophila* S2 cells (a gift from L. Teyton). Proteins were purified from culture supernatant by using Ni^{2+}-nitrilotriacetate resin affinity chromatography (Qiagen) followed by ion-exchange and size-exclusion chromatography (MonoQ 5/50 GL or 'MonoQ', Superdex-200 10/300 GL or 'S-200'). IE^k was preloaded with murine CLIP peptide in loading buffer (PBS plus 200 mM citrate buffer pH 5.1) and reloaded after size-exclusion S-200 chromatography (S-200) with fluorescent peptides for 1–5 days, purified with MonoQ and S-200. Peptide loading was dependent foremost on the duration of the CLIP peptide incubation and ranged from 40–85% as determined by spectrophotometry at 280, 552 and 647 nm. Because synaptic FRET yield depended on the surface density of fluorescent pMHC complexes but not on their loading degree, we conclude that the unlabelled fraction of bilayer-resident proteins present did not contain a significant amount of peptide-loaded complexes that had lost their fluorescent label (Supplementary Fig. 15). MCC (88–103, ANERADLIAYLKQATK), MCC(C) (ANERADLIAYLKQATKGGdSdC), T102S(C) (ANERADLIAYLKQASKGGdSdC), T102G(C) (ANERADLIAYLKQAGKGGdSdC), K99R(C) (ANERADLIAYLRQATKGGdSdC), MCC null(C) (ANERAELIAYLTQAAKGGGdSdC), β_2m(C) (dHdPdPdHdIdEIQMLKNGKKIPGGdSdC), ER60(C) (GdFdPdTIYFSPANKKLGGdSdC), K5(N) (dCdAdNdEdRdAdDdLIAYFKAATKdF) and K5(C) (dAdNdEdRdAdDdLIAYFKAATKdFGGdSdC) (T-cell epitopes underlined; d indicates D-amino acids) were synthesized by the PAN facility at Stanford, purified by C_{18} reverse-phase high-performance liquid chromatography (HPLC), conjugated with Cy3 or Cy5 maleimide, purified by HPLC and confirmed in identity by liquid chromatography–electrospray ionization mass spectroscopy. For scFv generation, mRNA was prepared from H57-597 hybridoma (American Type Culture Collection) to serve as a template for 5′ rapid amplification of cDNA ends (Invitrogen). V_H and V_L antibody domains were fused as illustrated in Supplementary Fig. 16 and mutagenized for J1, J2 and J3 generation (Quikchange; Stratagene). scFv refolded from inclusion bodies[25] were purified with S-200, labelled for 2 h with Cy3/Cy5 maleimide in the presence of 50 μM tris(2-carboxyethyl) phosphine hydrochloride (TCEP; Pierce) and monomeric scFv–dye conjugates were size-purified (S75). The label:protein stoichiometry ranged between 0.95 and 1.1 as determined by spectrophotometry at 280, 552 and 650 nm. Epitope specificity was confirmed by flow cytometry of labelled lymphocytes that had been freshly isolated from 5c.c7 TCR transgenic mice and through binding competition with unlabelled whole H57 antibody. Non-specific binding was less than 5% (Supplementary Fig. 17a). scFv stayed associated with cell-bound TCR, as shown (Supplementary Fig. 17b). Incubation of T cells with H57 scFv neither altered their dose–response proliferation to antigen (Fig. 4c) nor changed their calcium signalling in response to antigenic bilayers (Supplementary Fig. 18).

Preparation of planar glass-supported lipid bilayers. 1-Palmitoyl-2-oleoyl-*sn*-glycero-3-phosphocholine (POPC) (45 mg) and 6.9 mg of 1,2-dioleoyl-*sn*-glycero-3-[*N*(5-amino-1-carboxypentyl)iminodiacetic acid] succinyl[nickel salt] (Ni-DOGS NTA; Avanti Polar Lipids) were mixed in chloroform, dried under vacuum, resuspended in 10 ml of PBS and bath sonicated under argon at 120–170 W in a Sonicator 3000 system (Misonix). Vesicles were centrifuged (1 h, 37,000 r.p.m., 25 °C; 8 h, 4 °C, 43,000 r.p.m., in a TLA 100-2 rotor (Beckman)) to pellet non-unilamellar vesicles. No. 1 glass slides (24 mm × 50 mm German borosilicate; Menzel-Gläser) were treated with a 1:1 mixture of concentrated sulphuric acid and 30% hydrogen peroxide (both from Sigma-Aldrich) for 30 min, rinsed with doubly distilled or deionized water (Purelab Ultra; ELGA), dried in air and attached with epoxy glue to the bottom of 8-well or 16-well LabTek chambers (Nunc), from which the glass bottom had been removed, for 20 min. Slides were exposed to a tenfold diluted lipid suspension for 5 min and rinsed with PBS; His-tagged proteins were added for 1 h then rinsed with PBS. Typically, bilayers were used within 6 h, during which the recovery yield after photobleaching remained up to 90% and no loss in bilayer-associated protein could be detected. Protein density was determined by dividing bulk fluorescence by single-molecule fluorescence. Imaging was performed in HBSS containing 1% ovalbumin (Sigma-Aldrich). Before the addition of cells, IE^k/MCC(C)-Cy5 was observed as rapidly diffusing monomers: the single-molecule mobility was characterized by a diffusion constant $D_{free} = 0.680 \pm 0.013\ \mu m^2\ s^{-1}$ (30 molecules μm^{-2}, 37 °C) (Supplementary Fig. 19a). No oligomerized pMHC was detected up to a surface density of 500 molecules μm^{-2} with the TOCCSL ('thinning out clusters while conserving the stoichiometry of labelling') method[26] (Supplementary Fig. 19b).

Microscopy. Samples were illuminated in TIRF microscopy mode with an inverted microscope (200M; Axiovert) by means of a chromatically corrected objective (100×, numerical aperture 1.46, α-Plan Apochromat; Zeiss) and by using the 514-nm line (for Cy3 excitation) or the 647-nm line (for Cy5 excitation) of an argon ion gas (Stabilite 2017-AR) or krypton ion gas continuous-wave laser (Stabilite-KR; Spectra Physics) focused on the back focal plane of the objective. Acousto-optical modulators (AOM 1205C-2; Isomet) ensured rapid shuttering. Single fluorophores were excited with 1–5-ms light pulses at a power density of 1–5 kW cm^{-2} (within the linear range of excitation for Cy3 and Cy5; data not shown). We compared the calcium response of T cells to antigenic bilayers in the absence and presence of TIRF single-molecule exposure and found no difference (Supplementary Fig. 20). Using custom filter combinations (Z520/647 RPC and Z528/647M; Chroma; and 700-nm short pass; Newport) the fluorescence emission was separated from excitation light and split into two spectral channels by a dichroic wedge (1° separation; Chroma). Images were acquired with a slow-scan charge-coupled device camera (Micro Max 1300-PB; Princeton Instruments). Alternatively, emission was analysed with a Dual-View beam splitter (630dcxr, HQ575/40m, HQ680/50m; Optical Insights) and images were captured with a back-illuminated EMCCD Cascade II:512 camera (Roper Scientific) at a readout speed of 5 MHz and at full Electron Multiplying (EM) gain. The standard deviation of the mean fluorescence signal of test beads captured by this camera was less than 2% (Supplementary Fig. 21). At the highest frame rate (100 frames s^{-1}) there was no drift in the signal. Home-made software or Metamorph software (Molecular Devices) controlled image acquisition. Experiments shown in Fig. 2a, b (5c.c7 TCR–IE^k/MCC) and Fig. 2c (5c.c7 TCR–IE^k/MCC at 24, 28, 33 and 37 °C) as well as the 5c.c7 TCR–IE^k/MCC k_{off} measurements at 37 °C at pMHC densities of 6 and 150 MCC(C)-Cy5 molecules μm^{-2} (Table 1) were performed in Linz. All other imaging experiments were conducted at Stanford. The experiment shown in Fig. 4a was performed independently with both setups, with almost identical results.

Analysis of bulk FRET through FRET donor recovery after FRET acceptor bleaching. We measured the FRET yield of entire synapses or synaptic TCR microcluster of T cells labelled with H57 scFv-Cy3 (or H57 scFv-Cy5) in contact with bilayers that had been decorated with ICAM-1, B7-1 and IE^k/peptide-Cy5 (or IE^k/peptide-Cy3) by using the following recording sequence: a low-intensity Cy5 acquisition (to monitor the Cy5 signal) was followed by a low-intensity Cy3/FRET acquisition (to monitor the Cy3 and FRET signal before acceptor bleaching), followed by a high-intensity 647-nm bleach pulse (to ablate Cy5), a second Cy3/FRET acquisition (to monitor the Cy3 signal after acceptor bleaching and verify FRET ablation) and finally a low-intensity Cy5 acquisition (to verify Cy5 ablation). All light exposures were conducted in TIRF mode. The time between the beginning of the first Cy3/FRET acquisition before Cy5 ablation and the end of the second Cy3/FRET image after Cy5 ablation was less than 1 s. After subtraction of camera background, the Cy3 intensity before Cy5 ablation ($I_{before\ bleach}$) was subtracted from the Cy3 intensity after Cy5 ablation ($I_{after\ bleach}$). The difference ($I_{after\ bleach} - I_{before\ bleach}$) was then divided by $I_{after\ bleach}$ to obtain the FRET yield.

Analysis of smFRET. The raw FRET image (red emission channel at 514 nm excitation) was corrected for donor bleed-through (DB) and acceptor cross-excitation (ACE). DB, measured in the presence of donor fluorescence and in the absence of acceptor fluorescence, was 5.5% in Linz and 7.6% at Stanford. ACE was determined in the absence of donor fluorophores and in the presence of acceptor fluorophores for each experimental setting on a pixel-by-pixel basis. For the measurements of dissociation rate, smFRET events had to appear and disappear in single steps and co-localize with single-molecule acceptor events (Supplementary Figs 2–7). J1-Cy3 was employed at a J1-Cy3:TCR stoichiometry of less than 1:6 to attenuate donor bleed-through noise sufficiently. Before image acquisition, Cy5 was sufficiently photobleached to serve as a low-abundance species in the smFRET experiments. Unless otherwise indicated, IE^k/MCC(C)-Cy5 was applied at a density of 30 molecules μm^{-2}, under which conditions about 40% of synaptic IE^k/MCC(C)-Cy5 molecules are TCR-bound (M.A., unpublished observation). Typically, a set of two (514 and 647 nm excitation, 1 ms exposure, spaced by 1–5 ms) by ten images (split into a green and red emission channel, spaced by 5–2,000 ms) was recorded every 20–40 s. We also conducted single-molecule experiments with reversed label quantities (Cy3 in low abundance, Cy5 in high abundance; Supplementary Figs 8–10). These experiments gave rise to almost identical results for the measurements of 5c.c7 TCR–IE^k/MCC at 28 °C (a k_{off} of 0.55 s^{-1} versus a k_{off} of 0.575 s^{-1}). Because the diffusion rate of the bilayer-embedded IE^k was found to be significantly higher than that of the cell-bound TCR, and because the bilayer is an almost infinite reservoir of proteins, we purposely chose the much faster bleaching Cy5 as the bilayer-resident fluorophore (that is, as IE^k/MCC(C)-Cy5). This allowed us to undertake repetitive single-molecule acquisitions with intermittent (short) bilayer recovery periods on the same synapses.

***In situ* TCR–pMHC off-rate determination through smFRET analysis.** An example of the analysis is illustrated in Supplementary Fig. 22. Histograms of trace lengths of smFRET events were recorded for several acquisition time frames (Supplementary Fig. 22a) and converted into decay plots (Supplementary

Fig. 22b, c). Because FRET is susceptible to photobleaching, the observed decay O depends not only on the time passed (t) but also on the number of time frames (N) (as well as experimental setting-specific exposure time and power density) employed. Assuming stochastic photobleaching, $O(t,N)$ equals $D(t) \times B(N)$, with $D(t)$ representing time-dependent TCR–pMHC dissociation and $B(N)$ representing FRET photobleaching as a function of the number of time frames (as well as setting-specific exposure time and power density) employed. We first separated $B(N)$ from $O(t,N)$ by using very short time intervals where $D(t) \approx 1$ with $\lim_{t\to 0} O(N,t) = B(N)$ (for example, 15 ms at 24 °C or 5 ms at 37 °C). Subsequently, with the recorded $O(t,N)$ and known $B(N)$ and with $D(t) = O(t,N)/B(N)$, we derived $D(t)$ for longer time intervals relevant for time-dependent decay (Supplementary Fig. 22d; 50 ms and 100 ms for the 5c.c7 TCR–IE^k/MCC interaction at 37 °C, or 500 and 1,000 ms for measurements made at 24 °C).

Determination of effective 2D K_d values with quantitative labelling of the TCR. Density plots were determined by dividing the intensity of the Cy3 bulk fluorescent image (after acceptor bleaching), of the bulk Cy5 channel (before acceptor bleaching) and of the corrected FRET channel (before acceptor bleaching) through the average single-molecule intensity of the corresponding channel (Supplementary Fig. 11) and by adjusting molecule numbers for the effective pixel size ($1\,\mu m^2 = 42.51$ pixels). With these densities a 2D K_a plot was derived on a pixel-by-pixel basis. Multiplication of the 2D K_a plot with the synaptic k_{off} for 24 °C ($0.41\,s^{-1}$) gave rise to a 2D k_{on} plot.

Determination of effective 2D K_d values without quantitative labelling of the TCR. We employed TCR occupancy, which is proportional to the FRET yield, to determine effective 2D K_d values *in situ* through FRET measurements under conditions where TCR labelling is no longer saturating (for example, at higher temperatures).

Determination of TCR occupancy *a* from bulk FRET yield. The bulk FRET yield as measured through donor recovery after acceptor bleaching (with J1-Cy3 being the FRET donor and IE^k/MCC(C)-Cy5 being the FRET acceptor) is independent of the degree of TCR labelling, because it is a ratiometric parameter and is thus self-referential. It is also proportional to TCR occupancy a, the proportion of TCRs that are engaged with their ligands because dissociated scFv probes either diffuse out of the synapse or rebind unlabelled TCR at rates much higher than the rate of label dissociation. It can thus be described as

$$\text{FRET yield} \propto a = \rho(\text{TCR•pMHC})/\rho(\text{TCR}_{\text{total}}).$$

We quantified the linear relationship between bulk FRET yield and TCR occupancy experimentally and arrived at a proportionality factor $c = a/$(bulk FRET yield) of 1.955 (Supplementary Fig. 23b). For that, we imaged nascent synapses of T cells that had been quantitatively labelled with J1-Cy3 on ice and subsequently exposed to 20 °C for durations no longer than 150 s. At this point more than 95% of scFvs were still associated with the TCR. The recording sequence consisted of a low-intensity Cy5 acquisition (to monitor the Cy5 signal) followed by a low-intensity Cy3/FRET acquisition (to monitor the Cy3 and FRET signal before acceptor bleaching), a high-intensity 647-nm bleach pulse (to ablate Cy5), a second Cy3/FRET acquisition (to monitor the Cy3 signal after acceptor bleaching) and finally a low-intensity Cy5 acquisition (to verify Cy5 ablation). All exposures were conducted in TIRF mode. We then measured the FRET yield (determined through TCR–J1-Cy3 donor recovery after IE^k/MCC(C)-Cy5 acceptor bleaching, as described above) within individual TCR microclusters. We also directly determined the TCR occupancy a for the same microclusters. Quantitative and stoichiometric TCR labelling (see above) allowed us to deduce this parameter from the following relation: $a =$ (number of TCR–pMHC)/(number of all TCRs present) = [(corrected bulk FRET signal* before Cy5 ablation) × C/(average smFRET signal)] × [(average single-molecule Cy3 signal)/(bulk Cy3 signal* after Cy5 ablation) × C], with C being a constant and both bulk signals (*) acquired with the same excitation light exposure (emission separated using a beam splitter), = [(corrected bulk FRET signal before Cy5 ablation)/(bulk Cy3 signal after Cy5 ablation)] × [(average single-molecule Cy3 signal)/(average smFRET signal)]. The underlined ratio is a constant and depends only on two invariant parameters: first, the molecular FRET efficiency defined by the FRET system itself, and second, the acquisition hardware parameters defined by optical filters in the emission light train and the wavelength-dependent quantum efficiency of the camera. As can be deduced from the average single-molecule signals shown in Supplementary Fig. 11, it amounts to 2,978/2,054 = 1.45.

Hence the relation above simplifies to $a = 1.45 \times$ (corrected bulk FRET signal before Cy5 ablation)/(bulk Cy3 signal after Cy5 ablation). As shown in Supplementary Fig. 23b, the FRET efficiencies measured for individual TCR microclusters were then plotted against the TCR occupancies measured for the very same TCR microclusters to give rise to a linear fit ($R^2 = 0.91$) describing $a\,(\%) = FRET\,(\%) \times 1.955$.

Determination of the effective 2D K_d from TCR occupancy *a*. For the first-order reaction

$$\text{TCR} + \text{pMHC} \rightleftharpoons \text{TCR•pMHC} \quad (1)$$

we can formulate

$$2\text{D}\ K_d = \rho(\text{pMHC}_{\text{free}})\ \rho(\text{TCR}_{\text{free}})/\rho(\text{TCR•pMHC}) \quad (2)$$

From equation (1) we can formulate

$$\rho(\text{pMHC}_{\text{free}}) = \rho(\text{pMHC}_{\text{total}}) - \rho(\text{TCR•pMHC}) \quad (3)$$

and

$$\rho(\text{TCR}_{\text{free}}) = \rho(\text{TCR}_{\text{total}}) - \rho(\text{TCR•pMHC}) \quad (4)$$

Mobile bilayers provide an almost inexhaustible reservoir of T-cell ligands. Within the synapse, pMHC complexes therefore accumulate above $\rho(\text{pMHC}_{\text{initial}})$, the pMHC density before the addition of T cells, to an extent that is proportional to the degree of TCR binding and the formation of TCR–pMHC complexes. As a control, we estimated the potential synaptic enrichment of pMHC complexes through CD4 binding in the absence of TCR binding by monitoring the density of synaptic null ligands in the presence or absence of unlabelled agonist ligands, and found none (data not shown). Hence we can approximate

$$\rho(\text{pMHC}_{\text{total}}) = \rho(\text{pMHC}_{\text{initial}}) + \rho(\text{TCR•pMHC}) \quad (5)$$

Equation (2) can be reformulated through substitution to

$$\begin{aligned} 2\text{D}\ K_d &= \rho(\text{pMHC}_{\text{initial}}) \times [\rho(\text{TCR}_{\text{total}}) - \rho(\text{TCR•pMHC})]/ \\ &\quad \rho(\text{TCR•pMHC}) \\ &= \rho(\text{pMHC}_{\text{initial}}) \times [\rho(\text{TCR}_{\text{total}})/\rho(\text{TCR•pMHC}) - 1] \end{aligned}$$

and with

$$a = \text{TCR occupancy} = \rho(\text{TCR•pMHC})/\rho(\text{TCR}_{\text{total}})$$

to

$$2\text{D}\ K_d = \rho(\text{pMHC}_{\text{initial}}) \times (1/a - 1) \quad (6)$$

Equation (6) was then used to calculate effective 2D K_d values for individual TCR microclusters.

Calculation of 3D constants from 2D constants. To convert density-based (molecules μm^{-2}) values into concentration-based (molarity) values, we assumed the distance between the synaptic membranes in between which TCR–pMHC was binding to be 0.0134 μm. The 3D constants were derived from 2D constants as follows:

$$3\text{D}\ K_d = 2\text{D}\ K_d \times 10^{15}\,\mu m^2 l^{-1}/(N_A \times 0.0134\,\mu m^2)$$

(where N_A = Avogadro's constant)

$$\begin{aligned} &= 2\text{D}\ K_d \times 10^{15}\,\mu m^2 l^{-1}/(6.022 \times 10^{23}\ \text{molecules mol}^{-1} \times \\ &\quad 0.0134\,\mu m^2) \\ &= 2\text{D}\ K_d \times 1.239 \times 10^{-7}\,\text{M}\,\mu m^2\ \text{per molecule} \end{aligned}$$

and

$$3\text{D}\ k_{on} = 2\text{D}\ k_{on} \times 8.06 \times 10^6\,\text{M}^{-1}\,\mu m^{-2}\,\text{molecules}$$

Surface plasmon resonance (SPR) measurements. All SPR data were collected on a BiaCORE 3000 system (GE Healthcare) as described[10]. Soluble 5c.c7 TCR was expressed as a hybrid receptor consisting of the clonotypic 5c.c7 TCR Vα and Vβ domains fused to human LC13 TCR constant domain as described[27]. *Escherichia coli* inclusion bodies were refolded by fast dilution as described[28],

and purified on an Äkta system (GE Healthcare) by anion-exchange chromatography (MonoQ) and gel filtration (S-200). For binding studies, IE^k/MCC was expressed, refolded, purified, C-terminally biotinylated and immobilized on a streptavidin-coated BiaCORE chip (GE Healthcare) as described[29].

Reagents and cell cultures. Primary T cells were isolated from lymph nodes of 5c.c7 TCR and 2B4 TCR transgenic mice and cultivated as described[30]. The GK1.5 monoclonal antibody was purified from hybridoma culture supernatant. Cytochalasin D, latrunculin A and pp2 were purchased from Calbiochem, ovalbumin was from Sigma-Aldrich, and Cy3 maleimide and Cy5 maleimide were from GE Healthcare.

T-cell proliferation assay. Lymphocytes (10^4) that had been freshly isolated from $Rag^{-/-}$ 5c.c7 TCR transgenic mice, were pooled in a 96-well round-bottomed plate in a total volume of 100 µl with 5×10^5 irradiated (1,500 rad) splenocytes obtained from haplotype-matched B10.BR mice and exposed to MCC peptide and antibodies as indicated. After 48 h, cells were pulsed with 1 µCi [^{3}H]thymidine per well (100 µl) and incubated for a further 14 h. Incorporated [^{3}H]thymidine was quantified with the 1450 MicroBeta plate reader system (Perkin Elmer).

Ratiometric measurements of intracellular calcium levels. T cells were labelled in medium containing 5 µM Fura-2 acetoxymethyl ester (Invitrogen) between 22 and 25 °C for 30 min and washed in imaging buffer. Cell suspension (0.5 µl; 5×10^6 cells ml^{-1}) was carefully placed into close proximity with the bilayer to settle within 1 min. The Fura-2 signal was recorded immediately after addition of the cells and was averaged for about 1,000 cells per group. Imaging was performed with a 10× objective (10× Fluar, numerical aperture 0.5; Zeiss) to permit a greater field of view. Image analysis was performed as described.

25. Tsumoto, K. *et al.* Highly efficient recovery of functional single-chain Fv fragments from inclusion bodies overexpressed in *Escherichia coli* by controlled introduction of oxidizing reagent–application to a human single-chain Fv fragment. *J. Immunol. Methods* **219,** 119–129 (1998).
26. Moertelmaier, M., Brameshuber, M., Linimeier, M., Schütz, G. J. & Stockinger, H. Thinning out clusters while conserving stoichiometry of labeling. *Appl. Phys. Lett.* **87,** 263903 (2005).
27. Dai, S. *et al.* Crossreactive T cells spotlight the germline rules for αβ T cell-receptor interactions with MHC molecules. *Immunity* **28,** 324–334 (2008).
28. Tynan, F. E. *et al.* A T cell receptor flattens a bulged antigenic peptide presented by a major histocompatibility complex class I molecule. *Nature Immunol.* **8,** 268–276 (2007).
29. Wu, L. C., Tuot, D. S., Lyons, D. S., Garcia, K. C. & Davis, M. M. Two-step binding mechanism for T-cell receptor recognition of peptide MHC. *Nature* **418,** 552–556 (2002).
30. Huppa, J. B., Gleimer, M., Sumen, C. & Davis, M. M. Continuous T cell receptor signaling required for synapse maintenance and full effector potential. *Nature Immunol.* **4,** 749–755 (2003).

Please cite this article in press as: Hou et al., MAVS Forms Functional Prion-like Aggregates to Activate and Propagate Antiviral Innate Immune Response, Cell (2011), doi:10.1016/j.cell.2011.06.041

Cell

MAVS Forms Functional Prion-like Aggregates to Activate and Propagate Antiviral Innate Immune Response

Fajian Hou,[1] Lijun Sun,[1,3] Hui Zheng,[2] Brian Skaug,[1] Qiu-Xing Jiang,[2] and Zhijian J. Chen[1,3,*]
[1]Department of Molecular Biology
[2]Department of Cell Biology
[3]Howard Hughes Medical Institute
University of Texas Southwestern Medical Center, Dallas, TX 75390-9148, USA
*Correspondence: zhijian.chen@utsouthwestern.edu
DOI 10.1016/j.cell.2011.06.041

SUMMARY

In response to viral infection, RIG-I-like RNA helicases bind to viral RNA and activate the mitochondrial protein MAVS, which in turn activates the transcription factors IRF3 and NF-κB to induce type I interferons. We have previously shown that RIG-I binds to unanchored lysine-63 (K63) polyubiquitin chains and that this binding is important for MAVS activation; however, the mechanism underlying MAVS activation is not understood. Here, we show that viral infection induces the formation of very large MAVS aggregates, which potently activate IRF3 in the cytosol. We find that a fraction of recombinant MAVS protein forms fibrils that are capable of activating IRF3. Remarkably, the MAVS fibrils behave like prions and effectively convert endogenous MAVS into functional aggregates. We also show that, in the presence of K63 ubiquitin chains, RIG-I catalyzes the conversion of MAVS on the mitochondrial membrane to prion-like aggregates. These results suggest that a prion-like conformational switch of MAVS activates and propagates the antiviral signaling cascade.

INTRODUCTION

Innate immunity is an evolutionarily conserved defense mechanism against microbial infections (Iwasaki and Medzhitov, 2010; Ronald and Beutler, 2010; Takeuchi and Akira, 2010). In higher organisms, an antiviral innate immune response is triggered by the recognition of viral nucleic acids by germline-encoded pathogen recognition receptors, including Toll-like receptors (TLRs) and RIG-I-like receptors (RLRs) (Barbalat et al., 2011; Rehwinkel and Reis e Sousa, 2010). Several TLRs, including TLR3, 7, 8, and 9, detect viral RNA and DNA in the endosome, whereas RLRs bind to viral RNA in the cytoplasm. Both TLR and RLR pathways activate signaling cascades that lead to the production of an arsenal of effector molecules that suppress viral replication and assembly. Prominent among the antiviral molecules are type I interferons, including IFNα and IFNβ, which activate the JAK-STAT pathway to fight viral infection.

RLRs comprise RIG-I, MDA5, and LGP2, all of which contain an RNA helicase domain (Yoneyama and Fujita, 2009; Yoneyama et al., 2004). RIG-I also contains a C-terminal regulatory domain (RD) that binds to viral RNA harboring 5′-triphosphate (5′-pppRNA) (Hornung et al., 2006; Pichlmair et al., 2006). RIG-I and MDA5 detect distinct classes of RNA viruses (Kato et al., 2006). Both RIG-I and MDA5 contain two CARD domains in tandem at the N terminus, whereas LGP2 lacks the CARD domains. The binding of viral RNA to the C termini of RIG-I and MDA5 presumably induces a conformational change that exposes the N-terminal CARD domains, which interact with the CARD domain of the mitochondrial adaptor protein MAVS (also known as IPS1, VISA, or CARDIF) (Kawai et al., 2005; Meylan et al., 2005; Seth et al., 2005; Xu et al., 2005). MAVS then activates the cytosolic kinases IKK and TBK1, which activate the transcription factors NF-κB and IRF3, respectively. NF-κB and IRF3 translocate into the nucleus, where they function cooperatively to induce type I interferons and other antiviral molecules (McWhirter et al., 2005).

To understand the mechanism of signal transduction in the RIG-I pathway, we have recently established a cell-free system in which viral RNA triggers the activation of IRF3 and IKK in cytosolic extracts in the presence of mitochondria (Zeng et al., 2010). Using this system, we discovered that the CARD domains of RIG-I bind to unanchored K63 polyubiquitin chains and that this binding is important for RIG-I activation. The binding of full-length RIG-I to ubiquitin chains depends on ATP and 5′-pppRNA, suggesting that RIG-I activation involves sequential binding of viral RNA and unanchored K63 polyubiquitin chains to RIG-I RD and CARDs, respectively. We have also shown that mitochondria isolated from virus-infected cells can activate IKK and TBK1 in the cytoplasm and that this activity depends on MAVS on the mitochondrial membrane (Zeng et al., 2009). Interestingly, K63 polyubiquitination also plays an important role in TBK1 activation by MAVS.

The mechanism by which MAVS is activated by RIG-I and ubiquitin chains is still not understood. The nature of the active

form of MAVS has also remained a mystery. In this report, we show that MAVS forms very large aggregates after viral infection and that these aggregates are highly potent in activating IRF3 in the cytoplasm. Remarkably, these aggregates form self-perpetuating fiber-like polymers that can efficiently convert endogenous MAVS into functional aggregates. These properties closely resemble prions, which are infectious protein conformations found in pathological as well as physiological conditions (Chien et al., 2004; Halfmann and Lindquist, 2010; Tuite and Serio, 2010). Initially found to be the causative agent of fatal neurological diseases (Prusiner, 1998) —including Scrapies in sheep and goats, bovine spongiform encephalopathy (BSE, or "mad cow disease") in cattle, and Creutzfeldt-Jacob disease (CJD) in human—the prion PrP is the founding member of a growing list of proteins that can form self-perpetuating aggregates, several of which have evolved to serve physiological functions. For example, several prions in fungi regulate phenotypic switches that may confer selectable advantages (Halfmann and Lindquist, 2010). Thus, the prion-based conformational switch can be a robust epigenetic mechanism that regulates protein functions and cellular phenotypes. Properties of prions include fibrous aggregates, resistance to detergent and protease, and most importantly, the ability to "infect" the endogenous protein and convert the native conformation into fibrous aggregates. Strikingly, MAVS possesses all of these prion-like properties. The formation of MAVS aggregates leads to a gain of function, and the conformational switch is highly efficient and tightly regulated by viral infection. Also quite remarkably, in vitro incubation of RIG-I and mitochondria in the presence of K63 polyubiquitin chains efficiently converts endogenous MAVS into functional aggregates.

RESULTS

Viral Infection Induces the Formation of Large MAVS Signaling Complexes

To understand how MAVS is activated by viral infection, we used differential centrifugation to isolate crude mitochondria (P5) from HEK293T cells, which were infected with Sendai virus (+SeV) or were not infected (−SeV). The mitochondrial proteins were extracted in a buffer containing the nonionic detergent n-dodecyl beta-D-maltoside (DDM; 1%) and then fractionated by sucrose gradient ultracentrifugation. Aliquots of the fractions were analyzed by immunoblotting with a MAVS antibody, whereas other aliquots were incubated with ^{35}S-IRF3 and HEK293T cytosolic extracts in the presence of ATP. The dimerization of IRF3, which is caused by its phosphorylation by TBK1 and represents the hallmark of its activation, was measured by native gel electrophoresis (Panne et al., 2007; Yoneyama et al., 2002). As shown in Figure 1A, viral infection led to the formation of a very large complex containing MAVS, which activated IRF3 in the cytosol. This complex was much larger than 26S proteasome and sedimented toward the bottom of the centrifuge tube containing 50%–60% sucrose. We have previously shown that our MAVS antibody, which was raised against residues 131–291 of MAVS, detected two major bands on SDS-PAGE (Seth et al., 2005). The upper band represents full-length MAVS, whereas the lower band is a truncated form of MAVS, which lacks the N terminus but retains the C-terminal transmembrane domain. Interestingly, only the full-length MAVS formed a large complex capable of activating IRF3. Furthermore, almost all full-length MAVS shifted to the large complex in response to viral infection.

To visualize MAVS protein in cells, we expressed YFP-tagged MAVS in *Mavs*-deficient murine embryonic fibroblasts (MEFs) by retroviral transduction. Confocal fluorescence microscopy revealed that the staining pattern of YFP-MAVS overlapped with that of the mitochondrial marker Mitotracker in the absence of virus infection (Figure 1B). Strikingly, after infection with Sendai virus, YFP-MAVS appeared to form clusters that partially overlapped with Mitotracker, suggesting that MAVS forms aggregates in response to viral infection.

The large size of the active MAVS complex, together with our previous observation that MAVS in virus-infected cells is more resistant to detergent extraction (Seth et al., 2005), led us to test whether MAVS forms detergent-resistant aggregates. We employed a method called semidenaturing detergent agarose gel electrophoresis (SDD-AGE), which was previously used for the detection of prion-like structures (Alberti et al., 2009). In SDD-AGE, the crude mitochondria (P5) from cells infected with Sendai virus for different lengths of time were resuspended in a sample buffer containing 2% SDS and then separated on 1.5% agarose gel by electrophoresis in a running buffer containing 0.1% SDS (Figure 1C). Strikingly, a smear of SDS-resistant high-molecular weight MAVS aggregates appeared after 9 hr of viral infection, much like prions (Alberti et al., 2009). These aggregates were not detected in cells depleted of MAVS by RNAi, which blocked IRF3 activation by Sendai virus (Figure S1A available online). The kinetics of MAVS aggregate formation correlated with IRF3 activation by mitochondria from the virus-infected cells (Figure 1C). These results indicate that MAVS forms very large and highly active signaling complexes following viral infection.

In Figure 1C, we noted that our MAVS antibody could barely detect MAVS on SDD-AGE during the early time course of viral infection but was able to detect MAVS in the same samples when they were separated by the standard SDS polyacrylamide gel electrophoresis (SDS-PAGE). A major difference between SDD-AGE and SDS-PAGE is the presence of a reducing agent (β-mercaptoethanol or BME) in the latter, but not in the former, sample buffer. Interestingly, when crude mitochondria were resuspended in sample buffers containing different concentrations of BME followed by SDD-AGE, the smear of high-molecular weight MAVS aggregates disappeared (Figure 1D). These results suggest that the SDS-resistant MAVS aggregates may contain disulfide bonds and that the functional aggregates are preferentially detected by our MAVS antibody.

To determine whether reduction of the MAVS aggregates alters their activity and/or aggregation, we resuspended mitochondria from Sendai virus-infected cells in a buffer containing 1% DDM and 10 mM DTT and then fractionated the mitochondrial extracts by sucrose gradient ultracentrifugation. MAVS still sedimented as very large particles after the DTT treatment, and these particles were fully capable of activating IRF3 in the cytosol (Figure S1B). Control experiments showed that the DTT-treated particles in high-density sucrose fractions no longer formed detectable MAVS aggregates on SDD-AGE (Figure S1C). Thus,

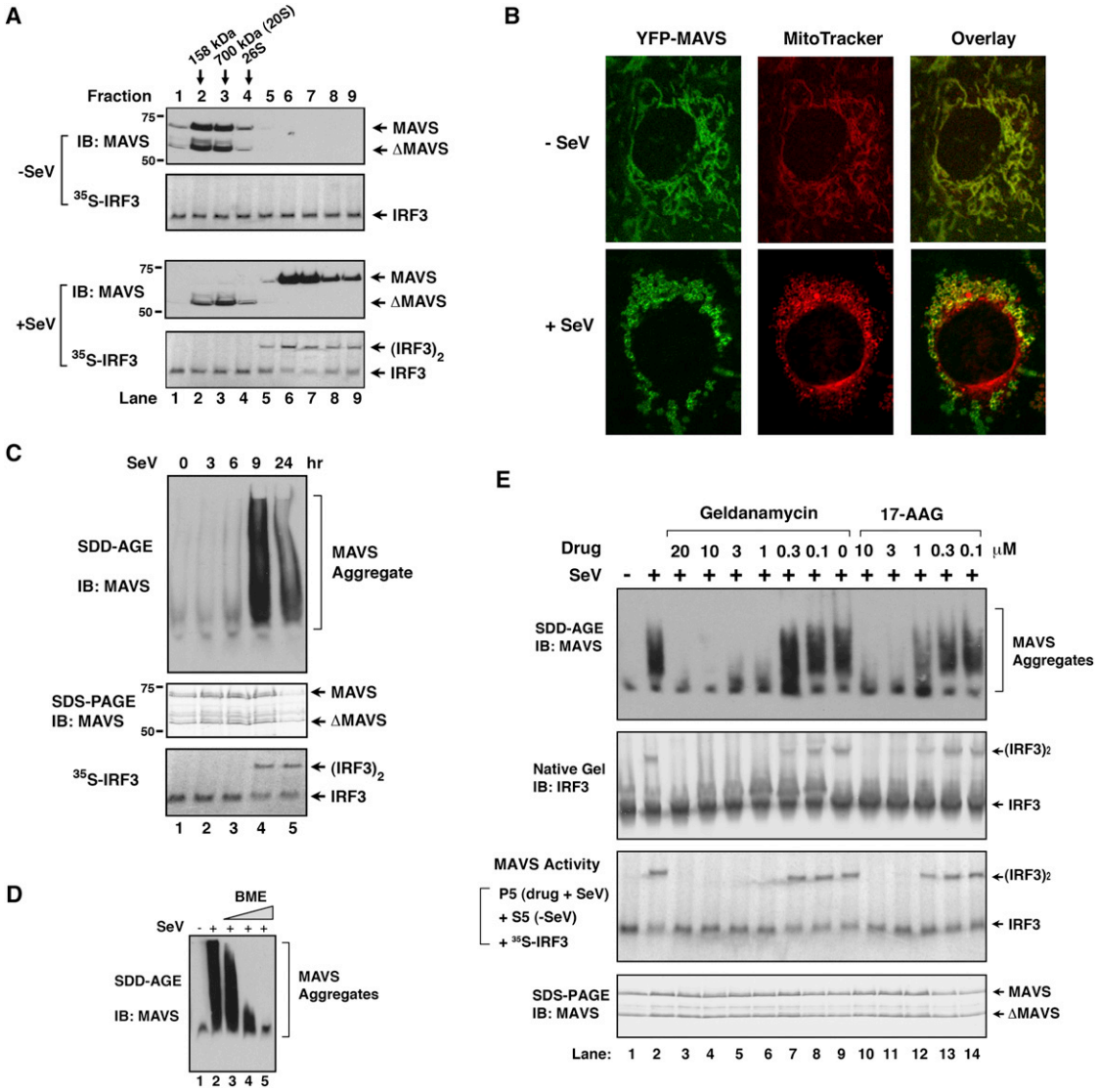

Figure 1. Viral Infection Induces the Formation of Large MAVS Particles that Activate IRF3

(A) Crude mitochondria isolated from HEK293T cells infected with Sendai virus for 14 hr (+SeV) or uninfected (−SeV) were solubilized in a buffer containing 1% DDM and then subjected to sucrose gradient ultracentrifugation. Aliquots of the fractions were immunoblotted with a MAVS antibody or incubated with ^{35}S-IRF3 and cytosolic extracts in the presence of ATP at 30°C for 60 min, followed by native gel electrophoresis and autoradiography. Arrows indicate the positions of proteins used as molecular size markers, including 20S and 26S proteasome. ΔMAVS denotes a truncated MAVS lacking the N terminus.

(B) YFP-MAVS was expressed in *Mavs*$^{-/-}$ MEF cells by retroviral transduction, and the cells expressing low levels of YFP-MAVS were sorted by FACS. These cells were infected with Sendai virus for 13 hr, stained with Mitotracker, and then visualized by confocal fluorescent microscopy. The images are representative of > 50% of the cells under examination.

(C) Crude mitochondrial extracts were prepared from HEK293T cells infected with Sendai virus for the indicated time, and then aliquots of the extracts were analyzed by SDD-AGE, SDS-PAGE, or IRF3 dimerization assays.

(D) Crude mitochondrial extracts were treated with or without β-mercaptoethanol (BME at 0.35, 3.5, and 35 mM), followed by SDD-AGE.

(E) HEK293T cells were treated with geldanamycin or 17-AAG at the indicated concentrations for 1 hr before Sendai virus infection. Ten hours later, the activation of endogenous IRF3 in the cytosolic extracts was analyzed by native gel electrophoresis. Mitochondria (P5) were prepared and analyzed by SDD-AGE or SDS-PAGE using a MAVS antibody. An aliquot of P5 was incubated with cytosolic extracts, ^{35}S-IRF3, and ATP followed by native gel electrophoresis to measure MAVS activity.

See also Figure S1.

DTT treatment prevented the detection of MAVS aggregates using the SDD-AGE assay but did not cause the breakdown of the MAVS aggregates, which could be isolated by ultracentrifugation. These MAVS aggregates were still active in causing IRF3 dimerization (Figure S1B). However, DTT treatment of cells blocked MAVS aggregation as well as IRF3 activation by Sendai virus (Figure S1D). This effect was more evident when DTT was applied during the early time course of virus infection than during

the late time course (Figure S1E). Thus, it is possible that disulfide bond formation facilitates MAVS aggregation, but the maintenance of the MAVS aggregates and its activity does not require the disulfide bonds. In any case, SDD-AGE without a reducing agent provides a sensitive assay for the detection of SDS-resistant, functional MAVS aggregates induced by virus infection.

Previous studies have identified several chemicals that inhibit IRF3 phosphorylation triggered by RNA viruses and poly[I:C] (Iwamura et al., 2001). Among these is the Hsp90 inhibitor geldanamycin, which inhibits IRF3 phosphorylation through an unknown mechanism. We found that geldanamycin and its analog (17-AAG), at concentrations that inhibited IRF3 activation, also blocked MAVS aggregation induced by Sendai virus (Figure 1E). Further, mitochondria isolated from cells treated with the drugs failed to activate IRF3 when incubated with cytosolic extracts. In contrast, cytosolic extracts from geldanamycin-treated cells could still support IRF3 activation when incubated with mitochondria from virus-infected cells (Figure S1F). Interestingly, the cytosolic extracts from Sendai virus-infected cells were refractory to activation by mitochondria from virus-infected cells (Figure S1F, lane 2), suggesting that some signaling proteins in the cytosol were desensitized following their activation. Taken together, these results suggest that geldanamycin and 17-AAG inhibit IRF3 activation by preventing MAVS aggregation on the mitochondria (see Discussion).

The Active MAVS Complex Is Composed of MAVS Polymers

To facilitate purification of the active MAVS complex, we generated a HEK293T cell line stably expressing Flag-MAVS. Analysis of the mitochondrial extracts from this cell line by sucrose gradient ultracentrifugation revealed that a fraction of Flag-MAVS formed a large complex that is capable of activating IRF3 dimerization even in the absence of viral infection, suggesting that overexpression caused a small fraction of Flag-MAVS to form the active complex (Figure S2A, top). Sendai virus infection caused the vast majority of MAVS to form the active complex (Figure S2A, bottom). However, despite much effort, we were unable to immunoprecipitate the active MAVS complex with antibodies against Flag or MAVS under native conditions. We therefore attempted to carry out immunoprecipitation under a partially denaturing condition that could maintain the activity of the MAVS complex. We found that, when the MAVS complex was solubilized in 2.5M guanidine-HCl and then dialyzed in a buffer containing 0.5 M guanidine-HCl, it could be immunoprecipitated with the Flag antibody, and the dialysis restored its ability to activate IRF3 (Figure S2B). Based on these experiments, we devised a protocol to purify the functional Flag-MAVS particles from Sendai virus-infected cells (Figure 2A and 2B). As a control, we also purified Flag-MAVS from uninfected cells. In both cases, silver staining of the purified particles revealed a predominant band that corresponded to Flag-MAVS itself (Figure 2B), which was verified by mass spectrometry and immunoblotting (data not shown). Importantly, only Flag-MAVS purified from the virus-infected cells formed aggregates and was capable of activating IRF3 when incubated with cytosolic extracts (Figure 2C). These results suggest that the active MAVS particles consist predominantly of the MAVS protein itself, which likely forms polymers.

Recombinant MAVS Protein Forms Fibrous Polymers that Activate IRF3

To test directly whether MAVS alone could form functional polymers, we attempted to express and purify recombinant MAVS protein in *E. coli*. Because full-length MAVS containing the C-terminal transmembrane domain (TM) was largely insoluble when expressed in *E. coli*, we expressed TM-deleted MAVS (MAVSΔTM) in HEK293T cells and then tested its ability to activate IRF3 in cytosolic extracts (Figures S3A and S3B). Interestingly, although the TM domain is absolutely required for MAVS to activate IRF3 and induce IFN in intact cells (Seth et al., 2005), in vitro incubation of MAVSΔTM with cytosolic extracts led to IRF3 dimerization (Figure S3B, lane 1). This result suggests that the activity of MAVSΔTM is blocked in intact cells by an unknown mechanism but unleashed in the in vitro assay (see below). We took advantage of this assay to test a panel of MAVS deletion mutants and found that the proline-rich region (residues 103–153) and the C terminus (residues 461–540) were dispensable for IRF3 activation, whereas the CARD domain was essential (Figure S3B). Based on these results, we expressed in *E. coli* a variant of MAVS lacking TM and proline-rich region as a fusion protein with Sumo, a ubiquitin-like protein that is known to facilitate expression of fusion partners in soluble forms. We purified this protein, termed Sumo-MAVS, to apparent homogeneity and found that it potently activated IRF3 in the cytosolic extracts (Figure S3C).

Interestingly, when Sumo-MAVS was analyzed by gel filtration on Superdex-200, a fraction of the protein eluted in the void volume, and these high-molecular weight forms activated IRF3 when they were incubated with cytosolic extracts (peak I; Figure 3A). In contrast, the low-molecular weight forms of Sumo-MAVS had no activity (peak II). Negative-stain electron microscopy of the protein particles showed that Sumo-MAVS in peak I formed large fiber-like polymers, whereas the protein in peak II formed much smaller particles with globular shapes (Figure 3B). When Peak II was stored at 4°C for 1 or 2 days, it gradually converted to peak I, indicating that the low-molecular weight forms of Sumo-MAVS spontaneously formed the fibrous polymers (Figure S3D). Removal of the Sumo tag caused the majority of MAVS to elute in peak I, which was also capable of activating IRF3 (data not shown). We also expressed and purified mouse MAVS lacking the TM domain as a His_6-tagged protein. The mouse MAVS protein also formed long fibers and were capable of activating IRF3 in cytosolic extracts (Figure 3C). The average diameter of the mouse MAVS fibers was smaller than that of the human Sumo-MAVS fibers, presumably because the presence of Sumo rendered the fibers thicker. These results suggest that the ability of MAVS to form fibrous polymers is evolutionally conserved and is independent of the purification tags.

MAVS Fibrils Have a Prion-like Activity that Converts Endogenous MAVS into Functional Aggregates

A hallmark of prions is their ability to convert endogenous proteins from their native conformations into prion-like fibrils. To test whether the MAVS fibrils have the prion-like activity, we

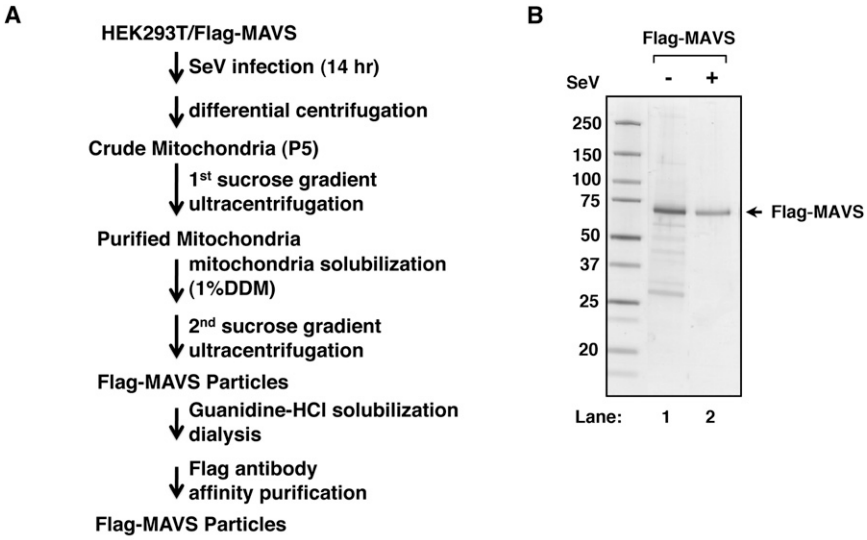

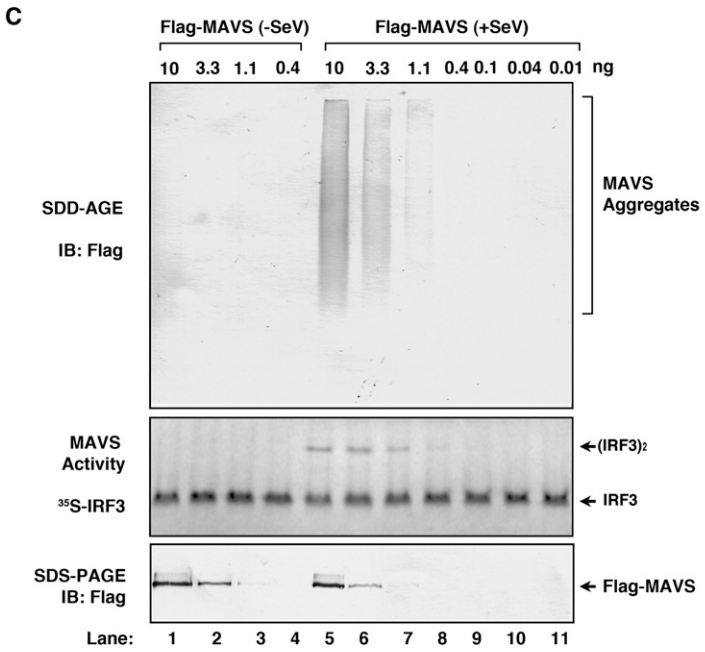

Figure 2. Purification of Active MAVS Particles

(A) A protocol for purification of active Flag-MAVS particles.

(B) Silver staining of Flag-MAVS purified from HEK293T cells infected with Sendai virus or not infected.

(C) IRF3 dimerization assay using purified Flag-MAVS shown in (B). MAVS was also analyzed by immunoblotting following SDD-AGE and SDS-PAGE.

See also Figure S2.

incubated the peak I and peak II fractions of Sumo-MAVS with mitochondria from HEK293T cells at room temperature for 30 min and then analyzed endogenous MAVS in the mitochondrial extracts by SDD-AGE (Figure 3D). Significantly, MAVS formed large aggregates after the mitochondria were incubated with peak I, but not peak II. Even highly diluted peak I (~80 ng/ml Sumo-MAVS; Figure 3D, lane 3), which was not detectable by the MAVS antibody, caused detectable aggregation of endogenous MAVS, suggesting a catalytic mechanism of this conformational conversion, which is reminiscent of prion-like infection. The mitochondria also gained the ability to activate IRF3 after incubation with peak I, and the activity was detectable with a concentration of peak I as low as 16 ng/ml (Figure 3E, lane 6). In contrast, peak II was unable to activate the mitochondria even at high concentrations. High concentrations of Peak I alone modestly activated IRF3, but this activity was significantly enhanced in the presence of mitochondria (e.g., compare lanes 3 and 4 in Figure 3E).

The CARD Domain of MAVS Forms Protease-Resistant Fibrils with a Prion-like Activity

Most prions form fiber-like structures that are resistant to protease digestion (Tuite and Serio, 2010). To determine whether the MAVS fibrils are resistant to proteolysis, we fractionated Sumo-MAVS on Superdex-200 and digested peak I and peak II with proteinase K (PK). Two prominent PK-resistant fragments appeared when peak I was digested for 2 hr, whereas such fragments were much less visible in the peak II sample (Figure 4A). The peak II sample contained a faint band that was relatively resistant to PK, and this band was identified as Hsp70 by mass spectrometry (Figure 4A, lanes 7–10; data not shown). Fractionation of the PK-digested Sumo-MAVS on Superdex-200 led to the separation of two peaks, with the first peak eluting in the void volume, similar to peak I of undigested Sumo-MAVS (Figure 4B). The second peak from the gel filtration column contained predominantly Hsp70, as determined by mass spectrometry (data not shown). Peak I contained a doublet with molecular weights of ~30 kDa. Both bands, designated as PK-MAVS, were excised for mass spectrometry, which identified multiple peptides of SUMO and the N terminus of MAVS, but none after residue 218 of MAVS (Figure S4A). These results suggest that PK-MAVS contains a fragment from Sumo and the N terminus of MAVS, including the entire CARD domain (Figure S4B). Negative-stain electron microscopy of PK-MAVS revealed that it formed long fibers with an average diameter of 12.6 ± 0.69 nm and an overall shape similar to that of the prion PrP (Figure 4C and Figure S4C).

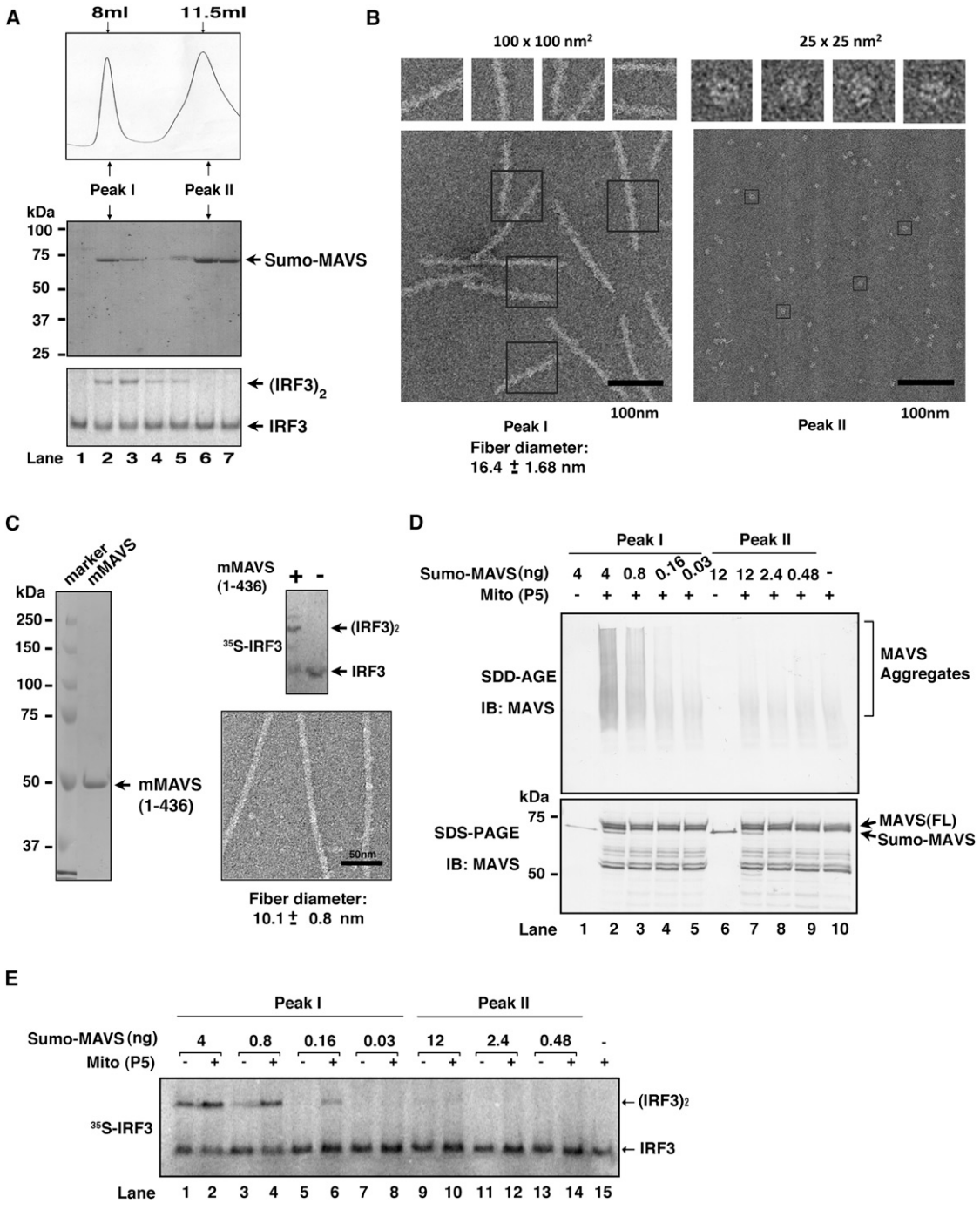

Figure 3. Recombinant MAVS Forms Fiber-like Polymers that Convert Endogenous MAVS into Functional Aggregates

(A) Sumo-MAVS lacking the proline-rich and TM domains was expressed and purified from *E. coli*, as described in Experimental Procedures, and then further fractionated by gel filtration on Superdex-200. Each fraction was analyzed by Coomassie blue staining and IRF3 dimerization assay.

(B) Two peaks of the Sumo-MAVS protein, as shown in (A), were imaged by electron microscopy using negative staining.

(C) Mouse MAVS lacking the TM domain was expressed as a His_6-tagged protein in *E. coli* and affinity purified. The purified protein was analyzed by IRF3 dimerization assay and electron microscopy.

(D) Peaks I and II of Sumo-MAVS, as shown in (A), were diluted 5-fold serially as indicated and then incubated with mitochondria from HEK293T cells (total volume: 10 μl). The mitochondria were solubilized in a buffer containing 1% DDM and then analyzed by SDD-AGE and SDS-PAGE with a MAVS antibody.

(E) The mitochondria incubated with Sumo-MAVS as described in (D) were subsequently incubated with ^{35}S-IRF3 and cytosolic extracts to measure IRF3 dimerization.

See also Figure S3.

The PK-MAVS fragment was incubated with mitochondria, which were subsequently analyzed for their ability to activate IRF3 and form aggregates (Figure 4D). Strikingly, following incubation with even highly diluted PK-MAVS (40–200 ng/ml; lanes 4 and 5), the mitochondria gained the ability to activate IRF3. Moreover, endogenous MAVS formed large aggregates, as revealed by SDD-AGE. In contrast, neither PrP fibers nor ubiquitin (as a globular protein control) caused MAVS aggregation or IRF3 activation even at much higher concentrations (Figure 4D, lanes 6–10). PK-MAVS alone did not activate IRF3 even at high concentrations (Figure 4D, lane 2), indicating that degradation of the C terminus, which contains binding sites for cytosolic signaling proteins such as TRAF2, TRAF3, and TRAF6 (Seth et al., 2005), abrogated its ability to activate IRF3. Thus, the PK-MAVS fibrils must act through endogenous MAVS to activate IRF3 in the cytoplasm. In support of this notion, mitochondria from cells depleted of MAVS by RNAi were unable to support IRF3 activation by PK-MAVS (Figure S4D). Reconstitution of MAVS-deficient MEF cells with full-length MAVS, but not a mutant lacking the CARD domain (MAVS-ΔCARD), supported IRF3 activation by PK-MAVS (Figure S4E). Furthermore, sucrose gradient ultracentrifugation revealed that full-length MAVS, but not MAVS-ΔCARD, formed high-molecular weight particles after the mitochondria were in contact with PK-MAVS (Figure 4E), indicating that the CARD domain of MAVS on the mitochondrial surface is required for its conversion to the active form by PK-MAVS. These results suggest that MAVS activation occurred through a prion-like conformational switch, which was triggered and templated by the PK-MAVS fibrils, likely through interaction between the CARD domains of the "infectious" agent (PK-MAVS) and that of endogenous MAVS. We estimated that ~1 ng of PK-MAVS caused the conversion of 16 ng of endogenous MAVS into functional aggregates within 30 min, again suggesting a prion-like catalytic mechanism.

Because PK-MAVS contains the CARD domain as well as other sequences (Figure S4A), we tested whether the CARD domain alone is sufficient to form functional fibrils. We expressed Flag-MAVS CARD-only (residues 1–100) in HEK293T cells and purified it to apparent homogeneity (Figure 4F). This protein alone did not activate IRF3, but its incubation with the mitochondria led to IRF3 activation. Electron microscopy showed that the CARD domain formed long fibers with an average diameter of 8.39 ± 1.1 nm. This diameter was smaller than that of PK-MAVS fibers, likely because it did not contain the extra N-terminal and C-terminal extension sequences found in PK-MAVS.

Our finding that the CARD domain of MAVS is capable of activating endogenous MAVS on the mitochondrial membrane in vitro is in contrast with our previous reports that the mitochondrial localization of MAVS is essential for its function in vivo (Li et al., 2005; Seth et al., 2005). Consistent with our previous reports, transfection of Flag-MAVS CARD-only into a HEK293T IFNβ-luciferase reporter cell line failed to induce the luciferase reporter or IRF3 dimerization (data not shown). When the MAVS CARD domain was fused to the TM domain, this fusion protein, termed mini-MAVS, strongly induced IFNβ and caused IRF3 dimerization (Figure S4F). Interestingly, depletion of endogenous MAVS by RNAi abrogated IFNβ induction by mini-MAVS (Figure S4F, lanes 5 and 6), indicating that mini-MAVS must act through endogenous MAVS to induce IFNβ. Thus, it appeared that endogenous MAVS on the mitochondria were prevented from being activated by the cytosolic MAVS CARD domain in intact cells through an unknown mechanism. Intriguingly, when the MAVS CARD domain is appended to the TM domain, it is highly potent in activating endogenous MAVS and IRF3, suggesting that the mitochondrial localization facilitates MAVS aggregation in cells.

MAVS Aggregates Recruit TRAF2 and TRAF6

Our observation that mini-MAVS requires endogenous MAVS to induce IFNβ suggests that the sequence between the CARD and TM domains of MAVS, which contain binding sites for TRAFs and other cytosolic signaling proteins, may mediate the recruitment of these proteins to MAVS aggregates. To test this possibility, we examined several signaling proteins that are known to be involved in NF-κB and IRF3 activation by immunoblotting following sucrose gradient ultracentrifugation of mitochondrial extracts (Figure 5). Interestingly, TRAF2 and TRAF6, but not IKKβ, TBK1, or IRF3, were found to sediment in the high-molecular weight fractions together with MAVS in response to Sendai virus infection (Figure 5A). The shifting of TRAF2 and TRAF6 to the high-molecular weight fractions was abrogated in cells depleted of MAVS by RNAi (Figure 5B). VDAC1, a mitochondrial outer-membrane protein, did not comigrate with MAVS after virus infection, suggesting that virus-induced formation of the MAVS complex does not lead to nonspecific aggregation of resident mitochondrial proteins. Further work is needed to understand how the recruitment of TRAF2, TRAF6, and potentially other signaling proteins to MAVS aggregates lead to the activation of NF-κB and IRF3.

RIG-I and K63 Polyubiquitin Promote MAVS Aggregation on the Mitochondrial Membrane

We have previously shown that RIG-I binds to K63 polyubiquitin chains through the N-terminal tandem CARD domains and that this binding is essential for IRF3 activation and interferon induction (Zeng et al., 2010). To determine whether RIG-I can promote MAVS aggregation in vitro, we incubated full-length RIG-I protein with mitochondria in the presence or absence of 5′-pppRNA and ubiquitin chains. Strikingly, after RIG-I was incubated with 5′-pppRNA, ATP, and K63-Ub4, it caused very rapid formation of MAVS aggregates on the mitochondrial membrane (Figure 6A). This activity required RNA and K63-Ub4 and was not induced by K48-Ub4 or mono-Ub. Overexpression of the RIG-I N terminus can activate IRF3 and induce IFN-β independently of viral RNA (Yoneyama et al., 2004). Purified GST-RIG-I(N) also caused robust MAVS aggregation when it was incubated with the mitochondria and K63-Ub4, but not K48-Ub4 or mono-Ub (Figure 6B). This activity did not require ATP and was unaffected by EDTA, which chelates magnesium (Figure 6B, lanes 10 and 11). The MAVS aggregates were not observed in cells treated with MAVS siRNA, confirming the identity of these aggregates (Figure S5A). Similar to RIG-I(N), overexpression of MDA5(N) in HEK293T cells led to aggregation of endogenous MAVS and dimerization of IRF3, and mutations of two conserved residues within the first CARD domain of MDA5 abrogated its ability to

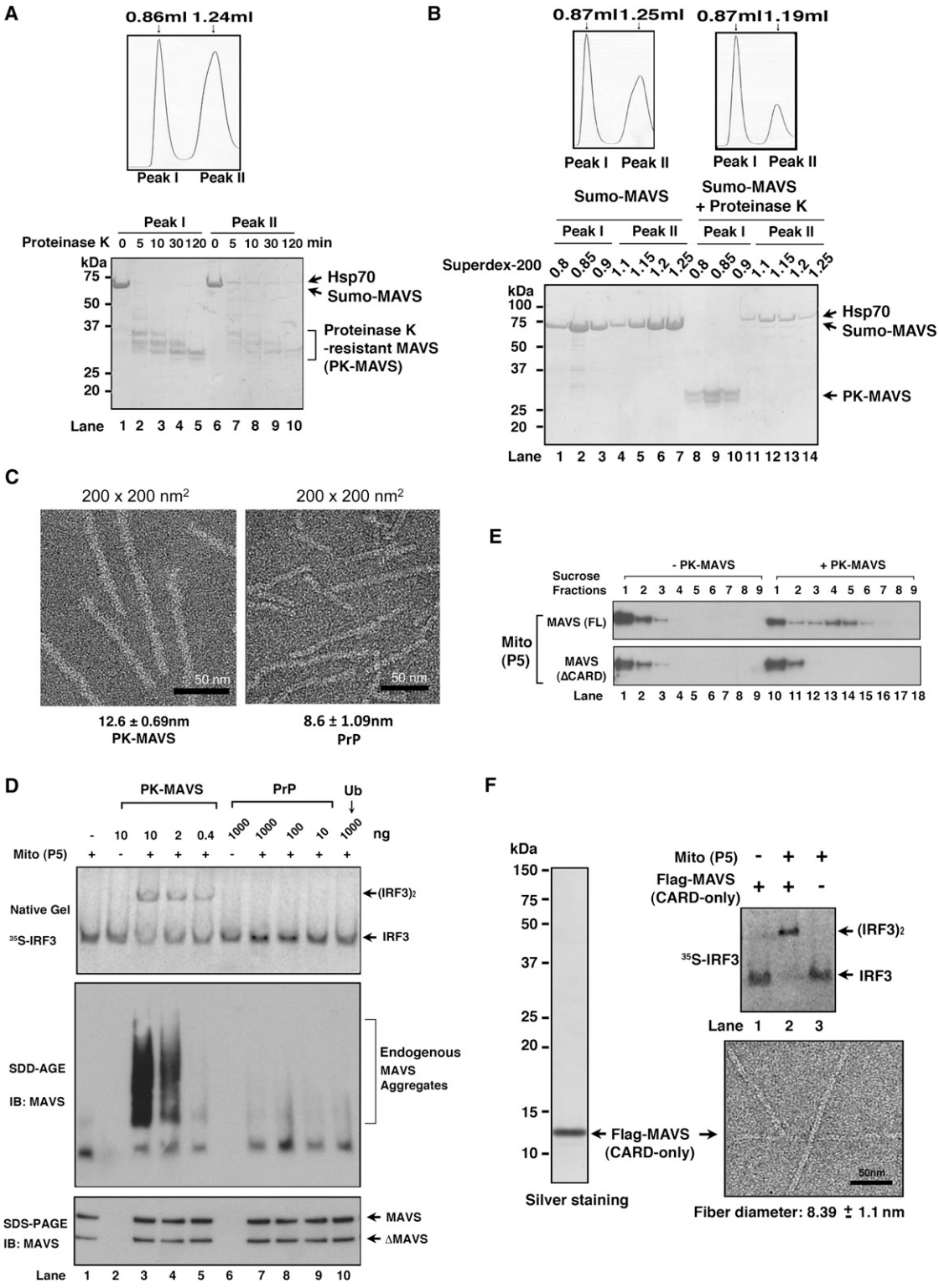

Figure 4. MAVS CARD Domain Forms Protease-Resistant Prion-like Fibers that Convert Endogenous MAVS into Functional Aggregates

(A) Sumo-MAVS in peaks I and II from Superdex-200 was digested with proteinase K (PK) for the indicated time at 22°C and then analyzed by Coomassie blue staining.

(B) Sumo-MAVS was treated with or without proteinase K for 1 hr and then fractionated on Superdex-200 (2.4 ml column). The fractions were analyzed by Coomassie blue staining. Mass spectrometry showed that the protease-resistant fragments in peak I contained the N terminus of MAVS, including the intact CARD domain (PK-MAVS; Figure S4A), and that the protease-resistant protein in peak II was Hsp70.

induce IRF3 dimerization and MAVS aggregation (Figure S5B). Titration experiments showed that ~60 nM K63-Ub4 (less for RIG-I[N]:K63-Ub4 complex) was able to convert ~130 nM MAVS into the aggregate forms within 30 min (Figure 6C, lane 8). Kinetic experiments showed that MAVS aggregation was evident after 2 min of exposure of the mitochondria to the RIG-I(N):K63-Ub4 complex (Figure 6D). SDD-AGE analysis showed that the SDS-resistant MAVS aggregates induced by RIG-I(N) and K63-Ub4 were sensitive to DTT treatment (Figure 6E, top); however, DTT treatment did not affect in vitro activation of MAVS by RIG-I(N) and K63-Ub4 (Figure 6E, bottom). Furthermore, the DTT-reduced MAVS still sedimented as high-molecular weight particles after sucrose gradient ultracentrifugation (Figure 6F). Thus, the MAVS aggregates induced in vitro by RIG-I and ubiquitin chains behaved similarly to those in cells triggered by viral infection.

DISCUSSION

We have previously shown that MAVS becomes more resistant to extraction with detergent from the mitochondrial membrane after viral infection (Seth et al., 2005). Recent microscopy studies show that MAVS redistributes in the mitochondria to form speckle-like aggregates in cells in response to viral infection (Onoguchi et al., 2010). In this report, we show that viral infection induces the formation of very large MAVS aggregates on the mitochondrial membrane. Importantly, we provide direct biochemical evidence that these aggregates are highly potent in activating IRF3 in cytosolic extracts. Furthermore, the aggregation of MAVS could be robustly induced in vitro by incubation of mitochondria with RIG-I and K63 ubiquitin chains. Most remarkably, our new data reveal that the CARD domains of MAVS form protease-resistant prion-like fibrils, which effectively convert endogenous MAVS on the mitochondria into functional aggregates. Based on these results and other published data, we propose a model of MAVS activation that involves the following steps (Figure 7): (1) RIG-I binds to viral RNA through the C-terminal RD domain and the helicase domain; (2) RIG-I hydrolyzes ATP, undergoes a conformational change, and forms a dimer that exposes the N-terminal CARD domains; (3) the CARD domains recruit TRIM25 and other ubiquitination enzymes to synthesize unanchored K63 polyubiquitin chains, which bind to the CARD domains; (4) the ubiquitin-bound CARD domains of RIG-I interact with the CARD domain of MAVS, which is anchored to the mitochondrial outer membrane through its C-terminal TM domain; (5) the CARD domain of MAVS rapidly forms prion-like aggregates, which convert other MAVS molecules into aggregates in a highly processive manner; and (6) the large MAVS aggregates interact with cytosolic signaling proteins, such as TRAFs, resulting in the activation of IKK and TBK1.

Prions are self-propagating protein aggregates that are best known for causing fatal neurodegenerative diseases (Prusiner, 1998). However, accumulating evidence through studies in fungi and other organisms suggests that prion-catalyzed conformational switches can regulate phenotypes in a way that is not detrimental and is, in some cases, beneficial to a cell or organism (Halfmann and Lindquist, 2010; Tuite and Serio, 2010). A recent example of beneficial prions is provided by the invertebrate *Aplysia* translation regulator CPEB, which forms self-sustaining polymers that contribute to long-term facilitation in sensory neurons (Si et al., 2003, 2010). Our finding that MAVS forms highly active, self-perpetuating fiber-like polymers provides another example of beneficial prions, in this case regulating mammalian antiviral immune defense.

MAVS shares many hallmarks of a prion, including: (1) the ability to ''infect'' the endogenous protein and convert it into the aggregate forms; (2) the formation of fiber-like polymers; (3) resistance to protease digestion; and (4) resistance to detergent solubilization. Surprisingly, although endogenous MAVS aggregates from virus-stimulated cells were resistant to 2% SDS as analyzed by SDD-AGE, these aggregates were sensitive to treatment with reducing agents such as DTT, suggesting disulfide bond formation within functional MAVS aggregates. Interestingly, disulfide bond formation has also been found in some prions, such as PrP (Stanker et al., 2010). However, even after DTT treatment, MAVS still sediments as very large and active particles after sucrose gradient ultracentrifugation, suggesting that disulfide bond formation is not essential to maintain the aggregation and activity of MAVS.

It remains to be determined whether MAVS forms one or a few very large aggregates or whether the aggregates are broken down to smaller fragments, which then form new ''seeds'' to multiply the aggregates. It would also be interesting to investigate how cells resolve these mitochondrial aggregates after an immune response is called into motion. Although there is evidence that MAVS is degraded by the ubiquitin-proteasome pathway (You et al., 2009), other mechanisms such as mitophagy or chaperone-mediated refolding are potentially involved in clearing the MAVS aggregates. Interestingly, we found that geldanamycin and its analog 17-AAG, which was previously known to inhibit IRF3 activation by RNA viruses, block MAVS aggregation. The dose response of the drugs shows an excellent correlation between MAVS aggregation and IRF3 dimerization, suggesting that MAVS aggregation is required for its function. It remains to be

(C) The fraction containing PK-MAVS shown in (B) (lane 9) and the prion PrP were imaged by electron microscopy using negative staining.
(D) PK-MAVS and PrP at the indicated amounts were incubated with the mitochondria from HEK293T cells at 22°C for 30 min (total volume: 10 μl). The mitochondria were subsequently incubated with ^{35}S-IRF3 and cytosolic extracts to measure IRF3 dimerization. Mitochondrial extracts were also analyzed by SDD-AGE and SDS-PAGE using a MAVS antibody, which reacts very weakly with PK-MAVS due to the removal of the epitopes.
(E) The CARD domain of MAVS is required for its conversion into aggregated forms by PK-MAVS. Full-length MAVS and MAVSΔCARD were expressed in *Mavs*$^{-/-}$ MEF cells by retroviral transduction. Mitochondria (P5) from these cells were incubated with or without PK-MAVS for 30 min before mitochondrial proteins were separated by sucrose gradient ultracentrifugation.
(F) The MAVS CARD domain was expressed in HEK293T cells as a Flag fusion protein and affinity purified. The purified protein was analyzed by silver staining, IRF3 dimerization assay, and electron microscopy.
See also Figure S4.

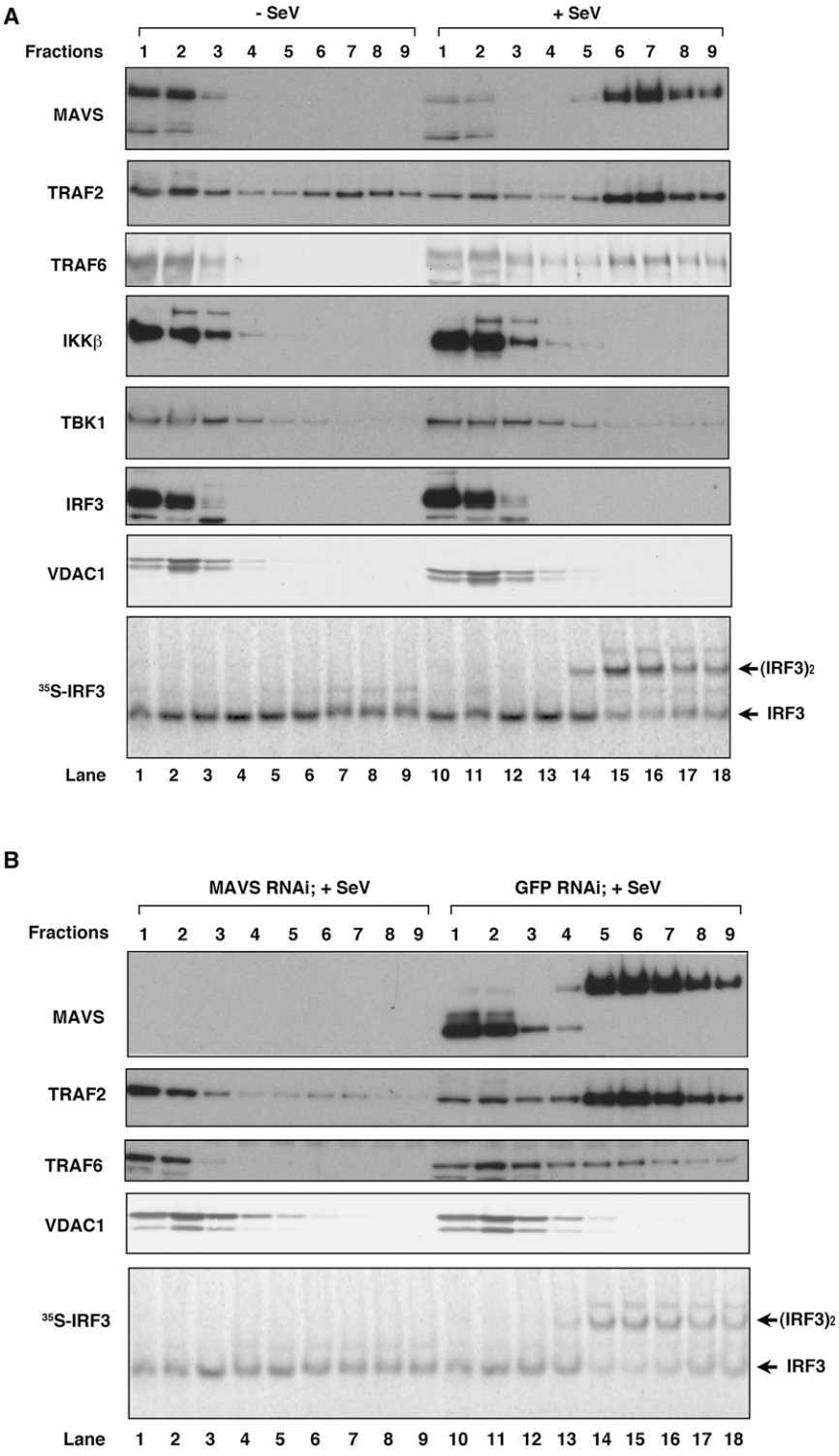

Figure 5. TRAF2 and TRAF6 Are Recruited to MAVS Aggregates in Response to Virus Infection

(A) Crude mitochondria (P5) were isolated from cells infected with Sendai virus or not infected, solubilized in 1% DDM, and then separated by sucrose gradient ultracentrifugation. Fractions were analyzed by immunoblotting with the indicated antibodies. Aliquots of the fractions were incubated with cytosolic extracts, ^{35}S-IRF3, and ATP followed by native gel electrophoresis.

(B) Similar to (A) except that cells were transfected with siRNA against MAVS or GFP (control) before virus infection.

determined whether the effect of geldanamycin is due to its inhibition of Hsp90. It is possible that Hsp90 facilitates ordered assembly of the functional MAVS fibers by preventing nonspecific aggregation.

Many prions form amyloids consisting predominantly of β sheets that may be detected with dyes such as Congo red (Chien et al., 2004; Sawaya et al., 2007). However, we have been unable to observe staining of MAVS aggregates with Congo red (data not shown). Like the CARD domains of other proteins, MAVS CARD forms a six-helix bundle (Potter et al., 2008). Likewise, other prion-genic proteins, such as the native form of PrP (PrPc), form α-helical folds before they are converted to the aggregate forms (Chien et al., 2004). Further studies are required to determine the atomic structure of the MAVS fibers and to understand how the fiber structure gains the competence to initiate downstream signaling. Importantly, MAVS fibers, but not PrP fibers, are able to induce endogenous MAVS aggregation, indicating specificity in this conformation-based mechanism of cell signaling.

CARD and CARD-like domains are present in a large variety of proteins, especially those involved in immune defense and cell death (Park et al., 2007). CARD domains are well known to mediate protein-protein interactions, and the CARD domains of RIG-I and MAVS likely mediate the interaction between these proteins. Surprisingly, our studies reveal that the CARD domains of RIG-I and MAVS have additional unique functions. The tandem CARD domains of RIG-I, but not the MAVS CARD, bind specifically to K63 polyubiquitin chains (Zeng et al., 2010). On the other hand, the CARD domain of MAVS, but not those of RIG-I, can form prion-like aggregates. The primary sequences of the CARD domains of RIG-I, MDA5, and MAVS are distantly related to conventional CARD domains found in other proteins. Interestingly, whereas the CARD domain of

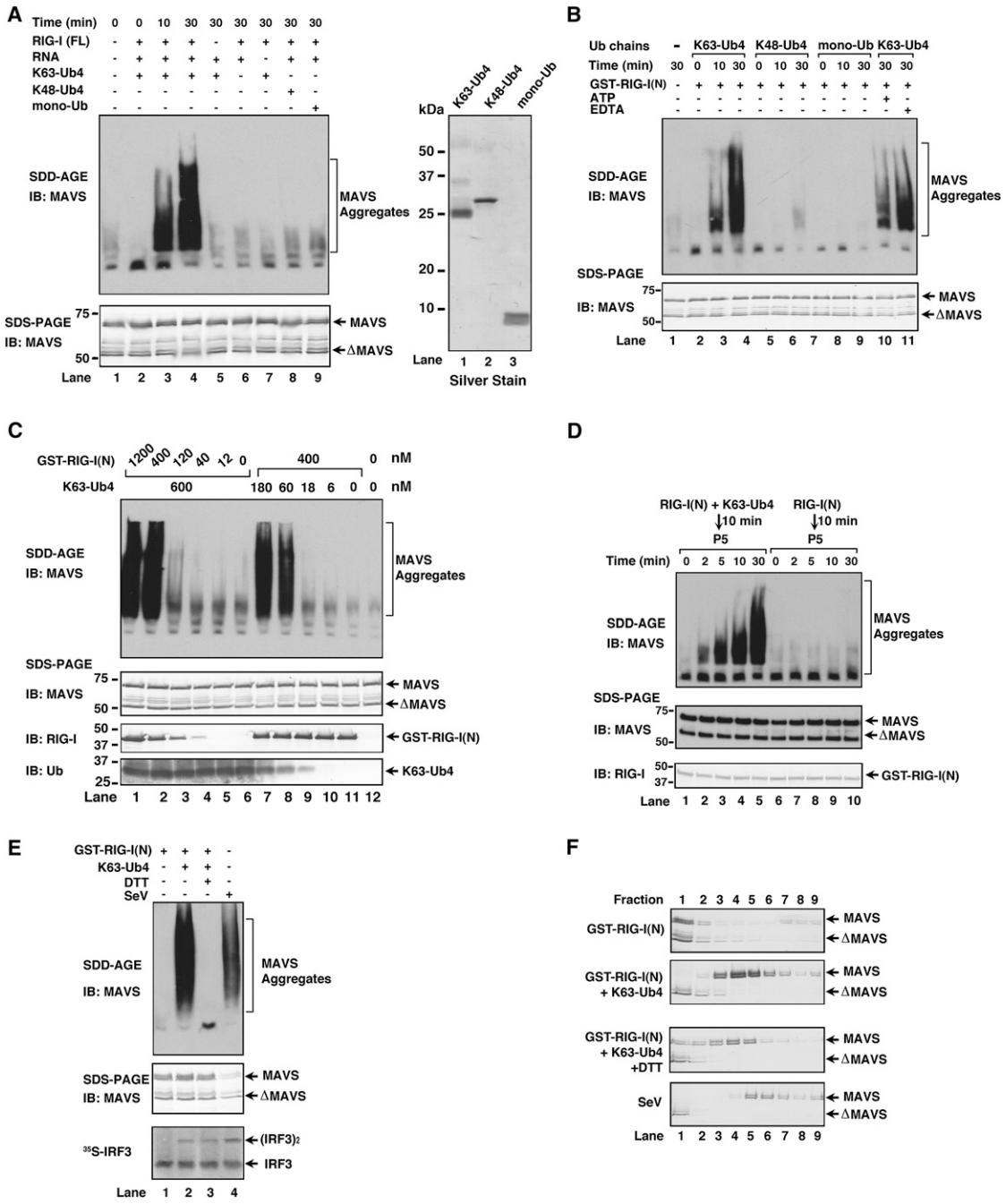

Figure 6. RIG-I and K63-Ub4 Induce MAVS Aggregation and Activation on the Mitochondrial Membrane

(A) Full-length RIG-I was incubated with 5′-pppRNA and/or ubiquitin chains as indicated at 22°C for 10 min. The mixtures were then incubated with mitochondria from HEK293T cells for 30 min before mitochondrial extracts were analyzed by SDD-AGE and SDS-PAGE. 0.25 μg of ubiquitin chains or mono-Ub was analyzed by silver staining (right).

(B) GST-RIG-I(N) was incubated with different ubiquitin chains at 22°C for 10 min in the presence or absence of ATP or EDTA as indicated. The mixture was then incubated with mitochondria from HEK293T cells for the indicated time, followed by analysis of the mitochondrial extracts using SDD-AGE and SDS-PAGE.

(C) Similar to (B) except that varying amounts of GST-RIG-I(N) and K63-Ub4 were used, and their incubation time with mitochondria was kept at 30 min.

(D) GST-RIG-I(N) was incubated with K63-Ub4 and then with mitochondria for the indicated time, followed by analysis of the mitochondrial extracts using SDD-AGE and SDS-PAGE.

(E) GST-RIG-I(N) was incubated with K63-Ub4 before incubation with mitochondria in the presence or absence of DTT. The mitochondrial extracts were analyzed by SDD-AGE, SDS-PAGE, and IRF3 dimerization assays. Mitochondria from Sendai virus-infected cells were used as a positive control.

(F) Mitochondrial extracts from (E) were fractionated by sucrose gradient ultracentrifugation followed by SDS-PAGE and immunoblotting with a MAVS antibody.

See also Figure S5.

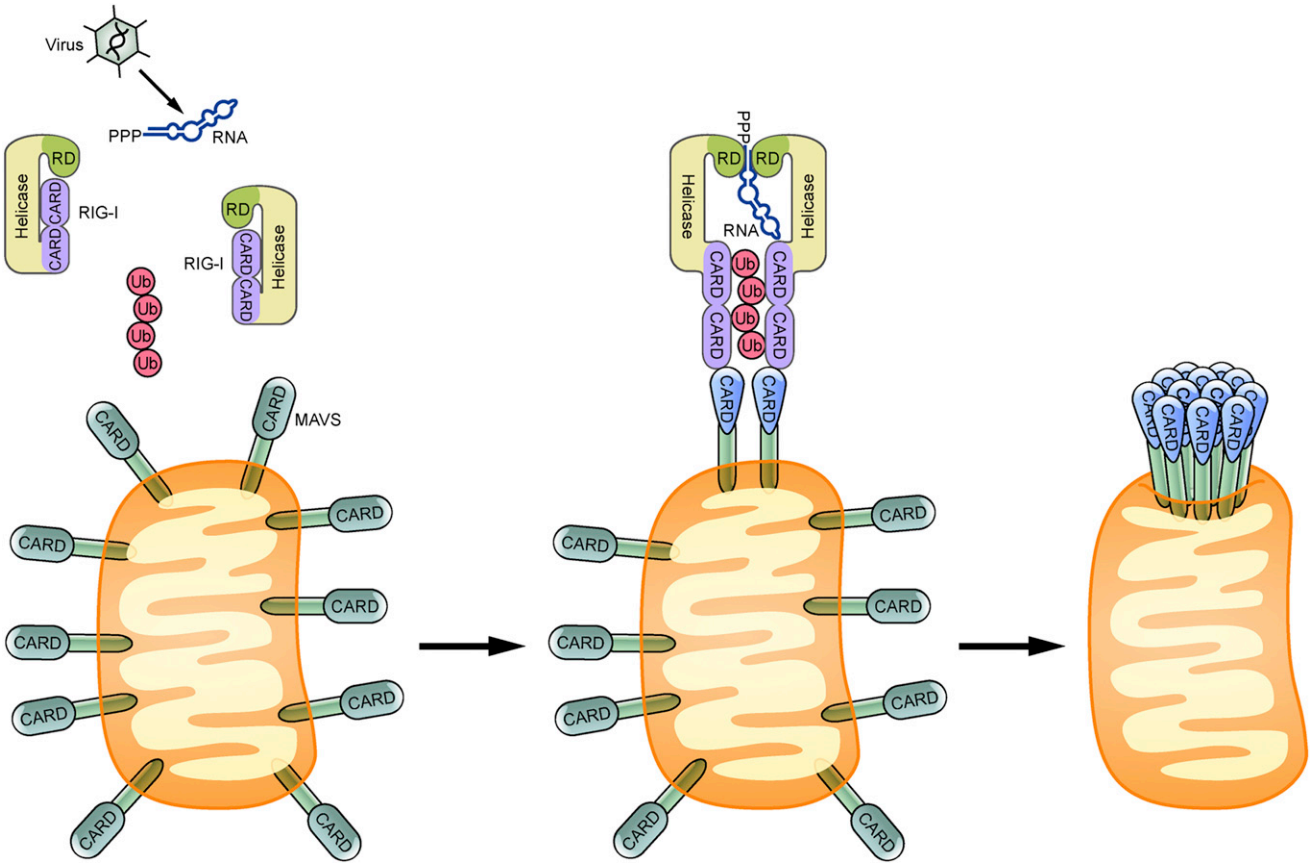

Figure 7. A Model of MAVS Activation Involving a Prion-like Conformational Switch Induced by RIG-I

Following sequential binding of RIG-I to viral RNA (5′-ppp RNA) and K63 ubiquitin chains, the CARD domains of RIG-I interact with the CARD domain of MAVS. This interaction induces a conformational change of the MAVS CARD (depicted by the change in color and shape of the CARD), which in turn converts other MAVS on the mitochondrial outer membrane into prion-like aggregates. These aggregates activate cytosolic signaling cascades to turn on NF-κB and IRF3, leading to induction of type I interferons and other antiviral molecules. MAVS on the mitochondrial membrane of uninfected cells may be a multimer but is depicted as a monomer for simplicity. Also not depicted is the possibility that MAVS on the surface of two adjacent mitochondria could aggregate through the N-terminal CARD domains, thereby propagating the antiviral signal between mitochondria.

MAVS shares very limited sequence homology with those of RIG-I and MDA5, the CARD domains of MAVS from different species have high degrees of sequence homology, and both mouse and human MAVS can form prion-like functional fibers (Figure 3). Thus, the MAVS CARD domain may have evolved to acquire the propensity to form prion-like aggregates, which obviously benefit the host organisms by mounting rigorous antiviral immune defense.

In cells, the CARD domain of MAVS must be appended to the mitochondrial targeting domain (TM) in order to induce IRF3 activation (Seth et al., 2005). In fact, overexpression of mini-MAVS that contains only the CARD and TM domains is sufficient to activate IRF3 and induce IFNβ in cells (Seth et al., 2005) (Figure S4F). The importance of the mitochondrial localization of MAVS is underscored by the fact that hepatitis C virus employs the viral protease NS3/4A to cleave MAVS off the mitochondrial membrane, thereby suppressing type I interferon production (Li et al., 2005; Meylan et al., 2005). Surprisingly, we found that recombinant MAVS lacking the TM domain (MAVSΔTM) could activate IRF3 when it is incubated with cytosolic extracts. Even a fragment containing only the CARD domain of MAVS is sufficient to form aggregates in vitro. The CARD domain aggregates can also activate IRF3 in cytosolic extracts, but in this case, the activity requires intact mitochondria containing endogenous MAVS (Figures 4D–4F). These biochemical results are consistent with our new finding that the induction of IFNβ by mini-MAVS in cells requires endogenous MAVS (Figure S4F). Taken together, our results suggest that the CARD domain of MAVS mediates aggregation, whereas the intervening sequence between CARD and TM domains is important for recruiting cytosolic signaling proteins to activate IKK and TBK1.

Though the vast majority of MAVS is located on the mitochondrial membrane, a very small fraction of MAVS is located on the peroxisomal membrane (Dixit et al., 2010). When MAVS was engineered to express predominantly on peroxisomal membrane, it failed to induce type I interferons but could still induce some antiviral genes, such as viperin, to inhibit viral infection through an interferon-independent mechanism. Our crude

mitochondrial preparation likely contains peroxisomes, raising the interesting possibility that a small fraction of MAVS that is located on the peroxisomal membrane may also form aggregates to induce viperin and other antiviral molecules.

Although overexpression of MAVS in cells is sufficient to cause its aggregation and induce type I interferons, the aggregation and activation of endogenous MAVS is tightly regulated by viral infection. We found that viral infection causes almost complete conversion of endogenous full-length MAVS into the aggregate forms. Such a highly efficient aggregation of MAVS can be reproduced in vitro by a simple incubation of mitochondria, RIG-I CARD domains, and K63-Ub4. Moreover, endogenous MAVS rapidly aggregates upon exposure of the mitochondria to the fibers consisting of MAVS CARD domain. These results suggest an amplification cascade in which the RIG-I:Ub chain complex causes some MAVS molecules to form aggregates, which then function as prion-like "seeds" to convert other MAVS molecules to form aggregates. Indeed, we found that substoichiometric amounts of K63-Ub4 and the MAVS CARD fibrils could cause almost complete conversion of endogenous MAVS into functional aggregates within 30 min in vitro, suggesting that the RIG-I:Ub chain complex and MAVS fibrils function like catalysts. This is consistent with our previous estimate that less than 20 molecules of viral RNA and K63 ubiquitin chains in a cell are sufficient to cause detectable IRF3 activation (Zeng et al., 2010). Thus, the RIG-I pathway appears to be highly sensitive to viral infection. Our finding of the prion-like conformational switch of MAVS provides a mechanism underlying this ultrasensitive and robust antiviral response.

EXPERIMENTAL PROCEDURES

In Vitro IRF3 Activation Assay

Crude mitochondria (P5) and cytosolic extracts (S5) were prepared by differential centrifugation. In brief, HEK293T cells were resuspended in Buffer A (10 mM Tris-HCl [pH 7.5], 10 mM KCl, 1.5 mM $MgCl_2$, 0.25 M D-mannitol, and Roche EDTA-free protease inhibitor cocktail) and then lysed by repeated douncing. After removing the cell debris by centrifugation at 1000 × g for 5 min, the supernatants were centrifuged at 10,000 × g for 10 min at 4°C to separate P5 and S5. ^{35}S-IRF3 was synthesized by in vitro translation in rabbit reticulocyte lysates (TNT; Promega) using pcDNA3-Flag-IRF3 as the template. P5 and S5 were incubated with ^{35}S-IRF3 and ATP, and then IRF3 dimerization was analyzed by native gel electrophoresis as described (Zeng et al., 2009).

Purification of Functional Flag-MAVS Particles from Virus-Infected Cells

HEK293T cells stably expressing Flag-MAVS (human) were infected with Sendai virus for 14 hr and then lysed in Buffer A by repeated douncing. After differential centrifugation as described above, mitochondria were further purified by sucrose density ultracentrifugation. In brief, mitochondria resuspended in Buffer B (20 mM HEPES [pH 7.4], 10% glycerol, 0.5mM EGTA, and 0.25 M D-mannitol) were loaded on top of a centrifuge tube containing 1 ml of 50% sucrose in phosphate-buffered saline (PBS) on the bottom layer and 1 ml of 40% sucrose in PBS on the top layer. After centrifugation at 100,000 × g for 30 min, mitochondria enriched at the interface of two layers were collected and solubilized with PBS containing 1% DDM. The mitochondrial lysate was loaded onto a sucrose gradient (30%–60%) and centrifuged at 170,000 × g for 2 hr. Nine fractions with equal volume were taken from the top to bottom of the tube. Fractions containing MAVS (corresponding to about 50%–60% sucrose) were pooled, and then guanidine-HCl was added to 2.5 M. The mixture was dialyzed against PBS containing 0.5 M Guanidine-HCl and 0.2% DDM overnight. Flag-MAVS was purified from the dialyzed mixture using anti-Flag (M2) agarose beads and eluted with the Flag-peptide (200 μg/ml). All procedures were performed at 4°C.

Purification of Flag-MAVS from uninfected cells was carried out as above except that, after isolation of mitochondria by sucrose gradient ultracentrifugation, the mitochondrial lysate was loaded on top of 40% sucrose cushion and centrifuged at 170,000 × g for 2 hr. The fraction above the sucrose cushion was incubated with anti-Flag (M2) agarose beads, followed by elution of Flag-MAVS with the Flag peptide.

Expression, Purification, and Protease Digestion of Recombinant MAVS Proteins

The bacterial expression vector pET-28a-His_6-Sumo-MAVS or pET14b-mMAVS was transformed into BL-21(pLys). Protein expression was induced with 0.2 mM IPTG at 18°C for 4 hr. After sonication in Buffer C (10 mM Tris-HCl [pH 8.0], 500 mM NaCl, 5 mM β-mercaptoethanol, 0.5 mM DTT, 5% glycerol, 0.5 mM PMSF, 0.5 mM AEBSF, and 10 mM imidazole), cell lysates were centrifuged at 50,000 × g for 30 min. His_6-Sumo-MAVS and His_6-mMAVS in the supernatant were purified using Ni-NTA beads, loaded onto a Hitrap-Q column, and then eluted with Buffer D (10 mM Tris [pH 7.5], 5% glycerol, 2 mM DTT, 1 mM EDTA, 0.5 mM PMSF, and 0.5 mM AEBSF) containing a gradient of NaCl from 0.1 M to 0.5 M. The fractions containing His_6-Sumo-MAVS, which was eluted with ~300 mM NaCl, were pooled and loaded onto a Superdex-200 gel filtration column equilibrated with Buffer E (10 mM Tris-HCl [pH 8.0], 150 mM NaCl, 1 mM DTT, 1 mM EDTA, 0.5 mM PMSF, and 0.5 mM AEBSF). FPLC (GE Healthcare) and a 24 ml Superdex-200 were used for large-scale purification, whereas a SMART or ETTAN purification system (GE Healthcare) and a 2.4 ml Superdex-200 column were used for small-scale purification.

Purified His_6-Sumo-MAVS was digested with proteinase K (mass ratio 50:1) at room temperature (~22°C) for the indicated time. To isolate the protease-resistant fragments, the reaction mixture was fractionated on Superdex-200 using the ETTAN system.

Flag-MAVS containing only the CARD domain was expressed in HEK293T cells by transient transfection of pcDNA3-Flag-MAVS-CARD. At 48 hr after transfection, cells were lysed in Buffer F (20 mM Tris-HCl [pH 8.0], 150 mM NaCl, 10% glycerol, 0.1% Triton X-100, 1 mM DTT, and protease inhibitors). After centrifugation at 10,000 × g for 10 min, Flag-MAVS CARD was absorbed on anti-Flag agarose beads and eluted with the Flag peptide. The eluate was further fractioned on Superdex-200 using the ETTAN system.

Semidenaturing Detergent Agarose Gel Electrophoresis

Semidenaturing detergent agarose gel electrophoresis (SDD-AGE) was performed according to a published protocol with minor modifications (Alberti et al., 2009). In brief, crude mitochondria (P5) were resuspended in 1 × sample buffer (0.5 × TBE, 10% glycerol, 2% SDS, and 0.0025% bromophenol blue) and loaded onto a vertical 1.5% agarose gel (Bio-Rad). After electrophoresis in the running buffer (1 × TBE and 0.1% SDS) for 35 min with a constant voltage of 100 V at 4°C, the proteins were transferred to Immobilon membrane (Millipore) for immunoblotting.

Induction of Endogenous MAVS Aggregation and Activation In Vitro

Crude mitochondria (P5) were isolated from HEK293T cells and incubated with indicated amounts of RIG-I, ubiquitin chains, or recombinant MAVS proteins at 22°C for different lengths of time. The reaction mixtures were centrifuged at 10,000 × g for 10 min, and then the pellets were analyzed by SDD-AGE and IRF3 dimerization assays. For ultracentrifugation analyses, the pellets were resuspended in PBS containing 1% DDM, treated with or without 10 mM DTT for 30 min, and then loaded on top of a sucrose gradient (20%–60%) and centrifuged at 170,000 × g for 2 hr.

SUPPLEMENTAL INFORMATION

Supplemental Information includes Extended Experimental Procedures and five figures and can be found with this article online at doi:10.1016/j.cell.2011.06.041.

ACKNOWLEDGMENTS

We thank Xiaomo Jiang for the MDA5 plasmids. This work was supported by grants from NIH (RO1-GM63692) and the Welch Foundation (I-1389). H.Z. was supported by a Welch Foundation grant (I-1684) and partially by a EUREKA grant from NIH (R01-GM88745 to Q.-X.J.). B.S is supported by an NIH predoctoral training grant (GM007062). Z.J.C. is an Investigator of Howard Hughes Medical Institute.

Received: February 8, 2011
Revised: May 19, 2011
Accepted: June 21, 2011
Published online: July 21, 2011

REFERENCES

Alberti, S., Halfmann, R., King, O., Kapila, A., and Lindquist, S. (2009). A systematic survey identifies prions and illuminates sequence features of prionogenic proteins. Cell *137*, 146–158.

Barbalat, R., Ewald, S.E., Mouchess, M.L., and Barton, G.M. (2011). Nucleic acid recognition by the innate immune system. Annu. Rev. Immunol. *29*, 185–214.

Chien, P., Weissman, J.S., and DePace, A.H. (2004). Emerging principles of conformation-based prion inheritance. Annu. Rev. Biochem. *73*, 617–656.

Dixit, E., Boulant, S., Zhang, Y., Lee, A.S., Odendall, C., Shum, B., Hacohen, N., Chen, Z.J., Whelan, S.P., Fransen, M., et al. (2010). Peroxisomes are signaling platforms for antiviral innate immunity. Cell *141*, 668–681.

Halfmann, R., and Lindquist, S. (2010). Epigenetics in the extreme: prions and the inheritance of environmentally acquired traits. Science *330*, 629–632.

Hornung, V., Ellegast, J., Kim, S., Brzózka, K., Jung, A., Kato, H., Poeck, H., Akira, S., Conzelmann, K.K., Schlee, M., et al. (2006). 5′-Triphosphate RNA is the ligand for RIG-I. Science *314*, 994–997.

Iwamura, T., Yoneyama, M., Yamaguchi, K., Suhara, W., Mori, W., Shiota, K., Okabe, Y., Namiki, H., and Fujita, T. (2001). Induction of IRF-3/-7 kinase and NF-kappaB in response to double-stranded RNA and virus infection: common and unique pathways. Genes Cells *6*, 375–388.

Iwasaki, A., and Medzhitov, R. (2010). Regulation of adaptive immunity by the innate immune system. Science *327*, 291–295.

Kato, H., Takeuchi, O., Sato, S., Yoneyama, M., Yamamoto, M., Matsui, K., Uematsu, S., Jung, A., Kawai, T., Ishii, K.J., et al. (2006). Differential roles of MDA5 and RIG-I helicases in the recognition of RNA viruses. Nature *441*, 101–105.

Kawai, T., Takahashi, K., Sato, S., Coban, C., Kumar, H., Kato, H., Ishii, K.J., Takeuchi, O., and Akira, S. (2005). IPS-1, an adaptor triggering RIG-I- and Mda5-mediated type I interferon induction. Nat. Immunol. *6*, 981–988.

Li, X.D., Sun, L., Seth, R.B., Pineda, G., and Chen, Z.J. (2005). Hepatitis C virus protease NS3/4A cleaves mitochondrial antiviral signaling protein off the mitochondria to evade innate immunity. Proc. Natl. Acad. Sci. USA *102*, 17717–17722.

McWhirter, S.M., Tenoever, B.R., and Maniatis, T. (2005). Connecting mitochondria and innate immunity. Cell *122*, 645–647.

Meylan, E., Curran, J., Hofmann, K., Moradpour, D., Binder, M., Bartenschlager, R., and Tschopp, J. (2005). Cardif is an adaptor protein in the RIG-I antiviral pathway and is targeted by hepatitis C virus. Nature *437*, 1167–1172.

Onoguchi, K., Onomoto, K., Takamatsu, S., Jogi, M., Takemura, A., Morimoto, S., Julkunen, I., Namiki, H., Yoneyama, M., and Fujita, T. (2010). Virus-infection or 5′ppp-RNA activates antiviral signal through redistribution of IPS-1 mediated by MFN1. PLoS Pathog. *6*, e1001012.

Panne, D., McWhirter, S.M., Maniatis, T., and Harrison, S.C. (2007). Interferon regulatory factor 3 is regulated by a dual phosphorylation-dependent switch. J. Biol. Chem. *282*, 22816–22822.

Park, H.H., Lo, Y.C., Lin, S.C., Wang, L., Yang, J.K., and Wu, H. (2007). The death domain superfamily in intracellular signaling of apoptosis and inflammation. Annu. Rev. Immunol. *25*, 561–586.

Pichlmair, A., Schulz, O., Tan, C.P., Näslund, T.I., Liljeström, P., Weber, F., and Reis e Sousa, C. (2006). RIG-I-mediated antiviral responses to single-stranded RNA bearing 5′-phosphates. Science *314*, 997–1001.

Potter, J.A., Randall, R.E., and Taylor, G.L. (2008). Crystal structure of human IPS-1/MAVS/VISA/Cardif caspase activation recruitment domain. BMC Struct. Biol. *8*, 11.

Prusiner, S.B. (1998). Prions. Proc. Natl. Acad. Sci. USA *95*, 13363–13383.

Rehwinkel, J., and Reis e Sousa, C. (2010). RIGorous detection: exposing virus through RNA sensing. Science *327*, 284–286.

Ronald, P.C., and Beutler, B. (2010). Plant and animal sensors of conserved microbial signatures. Science *330*, 1061–1064.

Sawaya, M.R., Sambashivan, S., Nelson, R., Ivanova, M.I., Sievers, S.A., Apostol, M.I., Thompson, M.J., Balbirnie, M., Wiltzius, J.J., McFarlane, H.T., et al. (2007). Atomic structures of amyloid cross-beta spines reveal varied steric zippers. Nature *447*, 453–457.

Seth, R.B., Sun, L., Ea, C.K., and Chen, Z.J. (2005). Identification and characterization of MAVS, a mitochondrial antiviral signaling protein that activates NF-kappaB and IRF 3. Cell *122*, 669–682.

Si, K., Choi, Y.B., White-Grindley, E., Majumdar, A., and Kandel, E.R. (2010). Aplysia CPEB can form prion-like multimers in sensory neurons that contribute to long-term facilitation. Cell *140*, 421–435.

Si, K., Lindquist, S., and Kandel, E.R. (2003). A neuronal isoform of the aplysia CPEB has prion-like properties. Cell *115*, 879–891.

Stanker, L.H., Serban, A.V., Cleveland, E., Hnasko, R., Lemus, A., Safar, J., DeArmond, S.J., and Prusiner, S.B. (2010). Conformation-dependent high-affinity monoclonal antibodies to prion proteins. J. Immunol. *185*, 729–737.

Takeuchi, O., and Akira, S. (2010). Pattern recognition receptors and inflammation. Cell *140*, 805–820.

Tuite, M.F., and Serio, T.R. (2010). The prion hypothesis: from biological anomaly to basic regulatory mechanism. Nat. Rev. Mol. Cell Biol. *11*, 823–833.

Xu, L.G., Wang, Y.Y., Han, K.J., Li, L.Y., Zhai, Z., and Shu, H.B. (2005). VISA is an adapter protein required for virus-triggered IFN-beta signaling. Mol. Cell *19*, 727–740.

Yoneyama, M., and Fujita, T. (2009). RNA recognition and signal transduction by RIG-I-like receptors. Immunol. Rev. *227*, 54–65.

Yoneyama, M., Suhara, W., and Fujita, T. (2002). Control of IRF-3 activation by phosphorylation. J. Interferon Cytokine Res. *22*, 73–76.

Yoneyama, M., Kikuchi, M., Natsukawa, T., Shinobu, N., Imaizumi, T., Miyagishi, M., Taira, K., Akira, S., and Fujita, T. (2004). The RNA helicase RIG-I has an essential function in double-stranded RNA-induced innate antiviral responses. Nat. Immunol. *5*, 730–737.

You, F., Sun, H., Zhou, X., Sun, W., Liang, S., Zhai, Z., and Jiang, Z. (2009). PCBP2 mediates degradation of the adaptor MAVS via the HECT ubiquitin ligase AIP4. Nat. Immunol. *10*, 1300–1308.

Zeng, W., Sun, L., Jiang, X., Chen, X., Hou, F., Adhikari, A., Xu, M., and Chen, Z.J. (2010). Reconstitution of the RIG-I pathway reveals a signaling role of unanchored polyubiquitin chains in innate immunity. Cell *141*, 315–330.

Zeng, W., Xu, M., Liu, S., Sun, L., and Chen, Z.J. (2009). Key role of Ubc5 and lysine-63 polyubiquitination in viral activation of IRF3. Mol. Cell *36*, 315–325.

EXTENDED EXPERIMENTAL PROCEDURES

Plasmids, Antibodies, and Proteins

cDNAs encoding full-length human MAVS in the mammalian expression vectors pEF-HA-IRES-Puro, pEF-Flag-IRES-Puro, and pcDNA3-Flag have been described previously (Seth et al., 2005). Deletion mutants of MAVS were constructed by PCR and then subcloned into appropriate expression vectors. For bacterial expression of Sumo-MAVS, a cDNA encoding MAVS lacking the proline-rich region (103–153) and the C terminus (461–540) was inserted into the BamHI and XhoI sites in a modified pET28a vector such that His_6 and Sumo tags were fused to the N-terminus of MAVS. The cDNA encoding mouse MAVS (1–436) was inserted between NdeI and BamHI sites of pET14b for bacterial expression of His_6-mMAVS. The baculoviral expression vector for full-length Flag-RIG-I, the bacterial expression vector for GST-RIG-I(N) and the mammalian expression vectors for mini-MAVS and MAVSΔ CARD have been described (Seth et al., 2005).

Antibodies against MAVS and RIG-I were generated in rabbits using recombinant proteins His_6-MAVS(131–291) and His_6-RIG-I(1–242), respectively, and affinity purified as previously described (Seth et al., 2005). Antibodies against IRF3 and ubiquitin were purchased from Santa Cruz Biotech, and the Flag antibody (M2) and M2-agarose were from Sigma. K63-Ub4 and K48-Ub4 were from Boston Biochem. Ubiquitin, proteinase K and other reagents were from Sigma unless otherwise indicated.

Cell Lines, Viral Infection, Transfection, RNAi, and Reporter Assays

HEK293T cells were transfected with pEF-Flag-MAVS-IRES-Puro and then selected in the presence of puromycin (1 μg/ml) to establish a clone stably expressing Flag-MAVS. Wild-type and $Mavs^{-/-}$ MEFs have been described (Sun et al., 2006). Viral infection was generally carried out using Sendai virus (Cantell strain; Charles River laboratories; 50 hemagglutinating-units per ml). Transfection, RNAi, IFNβ ELISA and IFNβ-luciferase reporter assays were carried out as previously described (Zeng et al., 2010).

Preparation of PrP Fibrils

PrP peptide (residue 102-126; from Bachem AG Hauptstrasse) was dissolved in PBS at a concentration of 2 mM and incubated at 22°C for 2 days before the fibrils were examined by EM and tested in functional assays.

Confocal Fluorescent Microscopy

YFP-MAVS was cloned into the retroviral vector pMMP412 and the retroviruses were prepared according to published methods (He and Ting, 2002). *Mavs*$^{-/-}$ MEFs were infected with the retroviruses, selected with puromycin (1 μg/ml), and the cells expressing low levels of YFP-MAVS were sorted by FACS (Moflo, Beckman Coulter). After infection with Sendai virus, the cells were incubated with Mitotracker before fixation at 4% paraformaldehyde. After 3 washes with PBS, the coverslip was mounted for imaging on LSM510 META laser scanning confocal microscope (Carl Zeiss MicroImaging, Inc).

Electron Microscopy

Copper grids (Ted Pella Inc.) coated with a layer of thin carbon film (5-10 nm) were rendered hydrophilic by glow-discharge in air. Two microliters of purified MAVS samples were loaded onto the grids, incubated for ~20 s, and stained with 6% ammonium molybdate containing 0.5% trehalose at pH 6.5-6.9. After air drying for several minutes, the grids were inserted into a JEOL 2200FS FEG electron microscope. Images were taken on Kodak SO-163 films in low-dose mode (~20 electron/Å^2) at 50,000 x with defocus level varying between −0.5 to −1.2 microns. Regular calibrations of the microscope magnifications found that the nominal 50,000x used here was always accurate within 3.0% error. The films were developed in full-strength D19 developer for 12 min at room temperature, and selected in an optical diffractometer. Micrographs showing no obvious drift or astigmatism were digitized in a Zeiss SCAI scanner with a 14 mm step size, corresponding to 2.8 Å/pixel at the specimen level.

Mass Spectrometry

Tandem mass spectrometry was performed using LTQ-XL (Thermo) coupled in-line with a nano-HPLC (Eksigent) according to the previously described method (Chiu et al., 2009).

SUPPLEMENTAL REFERENCES

Chiu, Y.H., Macmillan, J.B., and Chen, Z.J. (2009). RNA polymerase III detects cytosolic DNA and induces type I interferons through the RIG-I pathway. Cell *138*, 576–591.

He, K.L., and Ting, A.T. (2002). A20 inhibits tumor necrosis factor (TNF) alpha-induced apoptosis by disrupting recruitment of TRADD and RIP to the TNF receptor 1 complex in Jurkat T cells. Mol. Cell. Biol. *22*, 6034–6045.

Seth, R.B., Sun, L., Ea, C.K., and Chen, Z.J. (2005). Identification and characterization of MAVS, a mitochondrial antiviral signaling protein that activates NF-kappaB and IRF 3. Cell *122*, 669–682.

Sun, Q., Sun, L., Liu, H.H., Chen, X., Seth, R.B., Forman, J., and Chen, Z.J. (2006). The specific and essential role of MAVS in antiviral innate immune responses. Immunity *24*, 633–642.

Zeng, W., Sun, L., Jiang, X., Chen, X., Hou, F., Adhikari, A., Xu, M., and Chen, Z.J. (2010). Reconstitution of the RIG-I pathway reveals a signaling role of unanchored polyubiquitin chains in innate immunity. Cell *141*, 315–330.

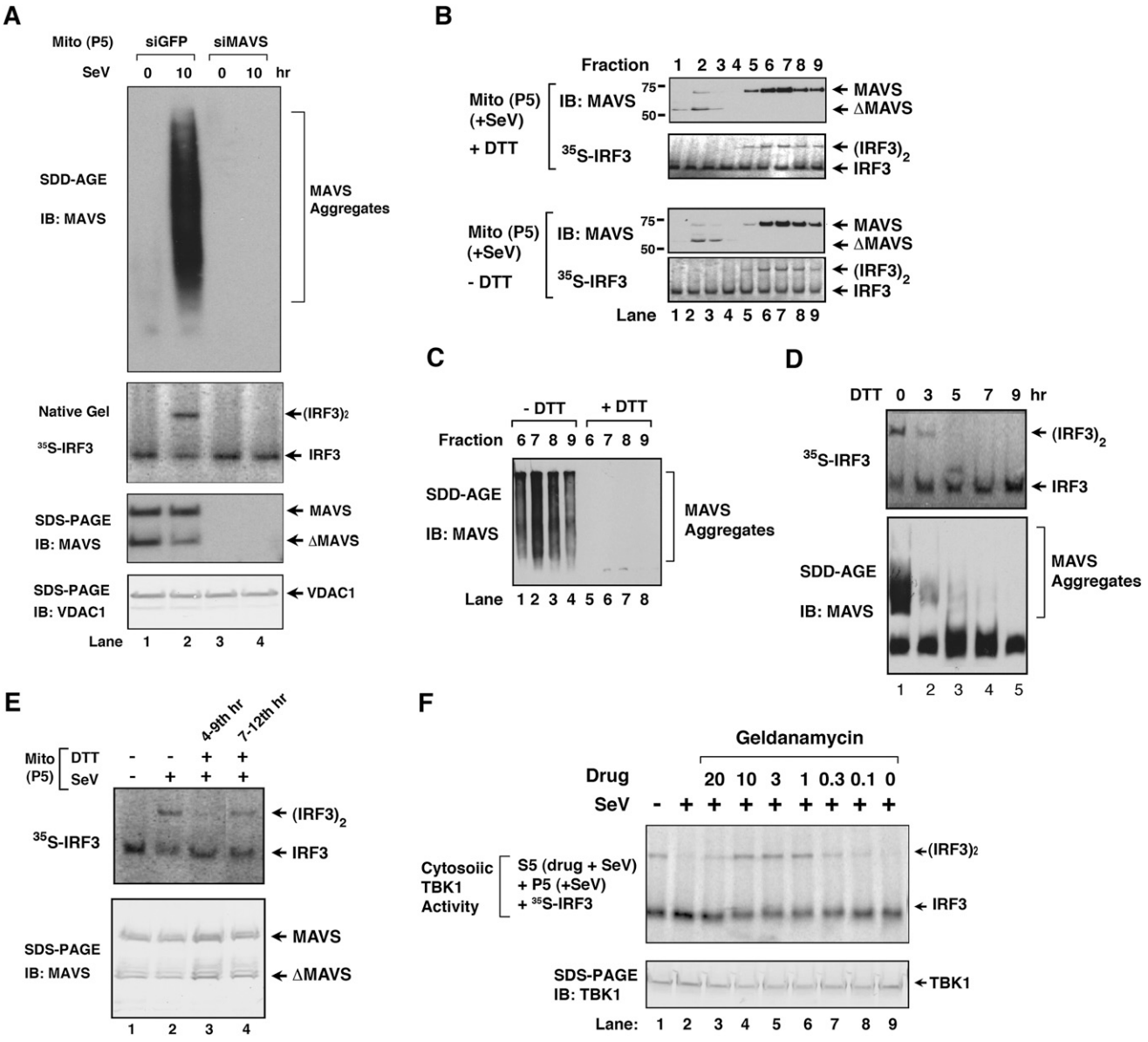

Figure S1. Virus-Induced Aggregation of MAVS, Related to Figure 1

(A) siRNA oligos targeting MAVS or GFP (control) were transfected into HEK293T cells, which were subsequently infected with Sendai virus for 10 hr. Mitochondria (P5) isolated from these cells were incubated with cytosolic extracts, ^{35}S-IRF3 and ATP followed by native gel electrophoresis. Aliquots of the mitochondrial extracts were separated by SDD-AGE or SDS-PAGE and then detected by immunoblotting with antibodies against MAVS or VDAC1.

(B) Crude mitochondrial extracts from Sendai virus-infected HEK293T cells were treated with or without 10 mM DTT for 30 min, then subjected to sucrose gradient ultracentrifugation, followed by MAVS immunoblotting and IRF3 dimerization assays.

(C) Aliquots of the high molecular weight fractions shown in (B) were analyzed by SDD-AGE.

(D) HEK293T cells were treated with 10 mM DTT for the indicated time while being infected with Sendai virus for 9 hr. Mitochondria (P5) were prepared to measure MAVS activity and aggregation by IRF3 dimerization and SDD-AGE assay, respectively.

(E) At 4th (lane 3) and 7th (lane 4) hours after infection of HEK293T cells with Sendai virus, DTT was added to the cells and the incubation continued for another 5 hr before mitochondria were isolated to measure MAVS activity.

(F) HEK293T cells were treated with different concentrations of geldanamycin and infected with Sendai virus as shown in Figure 1E. The cytosolic extracts were then incubated with mitochondria from Sendai virus-infected cells together with ^{35}S-IRF3 and ATP, followed by native gel electrophoresis.

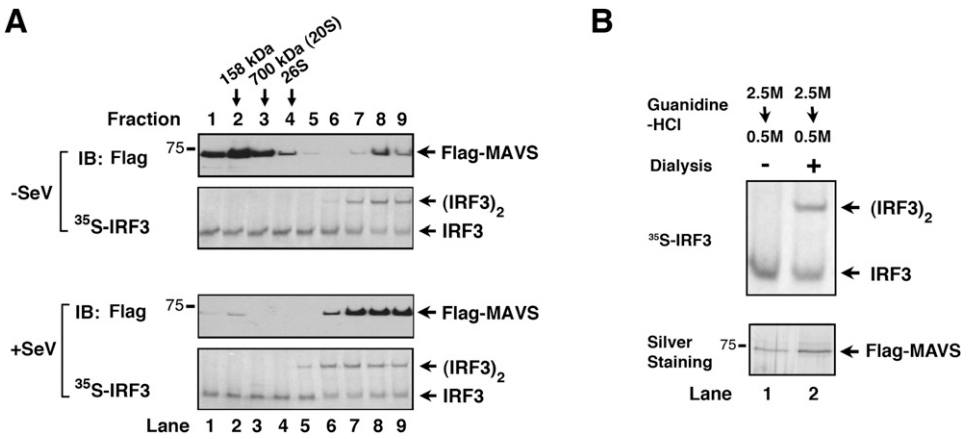

Figure S2. Establishing Conditions for the Purification of Functional MAVS Particles, Related to Figure 2

(A) Crude mitochondria were prepared from HEK293T-Flag-MAVS stable cells, which were infected with Sendai virus for 14 hr or uninfected. The mitochondrial extracts were fractionated by sucrose gradient ultracentrifugation, and the fractions were analyzed by MAVS immunoblotting or IRF3 dimerization assays.

(B) Guanidine-HCl was added to mitochondrial extracts from virus infected cells at a final concentration of 2.5M, then diluted to 0.5M directly (lane 1) or dialyzed against a buffer containing 0.5M guanidine-HCl (lane 2). Flag-MAVS was then affinity purified and analyzed by IRF3 dimerization assay and silver staining.

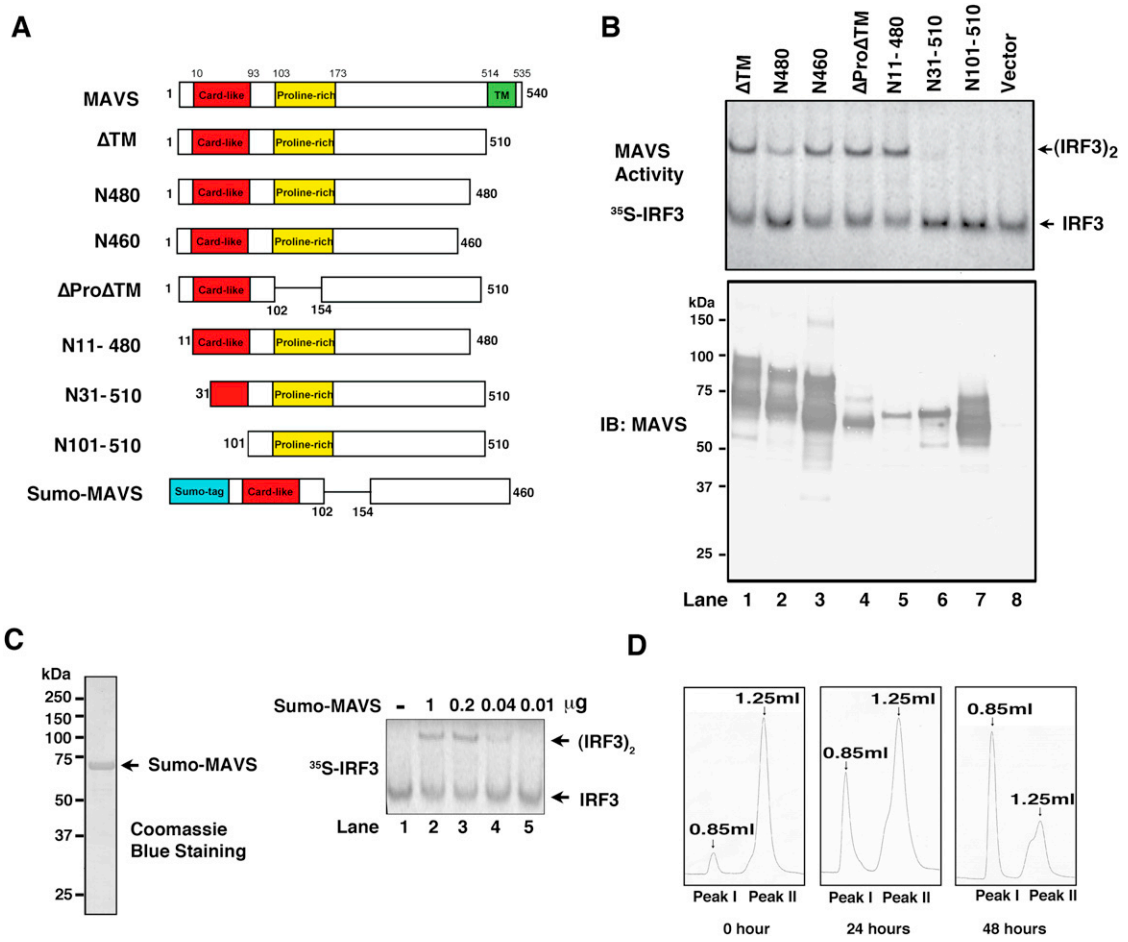

Figure S3. Structural and Functional Analyses of MAVS, Related to Figure 3

(A) Diagrams of MAVS domains and deletion mutants.

(B) HA-tagged MAVS deletion mutants as depicted in (A) were expressed in HEK293T cells and then the cytosolic extracts were incubated with ^{35}S-IRF3 and ATP, followed by native gel electrophoresis and autoradiography. Aliquots of the MAVS deletion mutants were analyzed by immunoblotting.

(C) Sumo-MAVS was expressed in *E. coli* as a His_6-tagged protein and purified using Ni-NTA followed by mono-Q columns. 1 μg of the purified protein was used for Commassie blue staining, whereas different amounts as indicated were used for IRF3 dimerization assay.

(D) Peak II shown in Figure 3A was stored at 4°C for the indicated time, then analyzed by gel filtration on Superdex-200 using the SMART purification system.

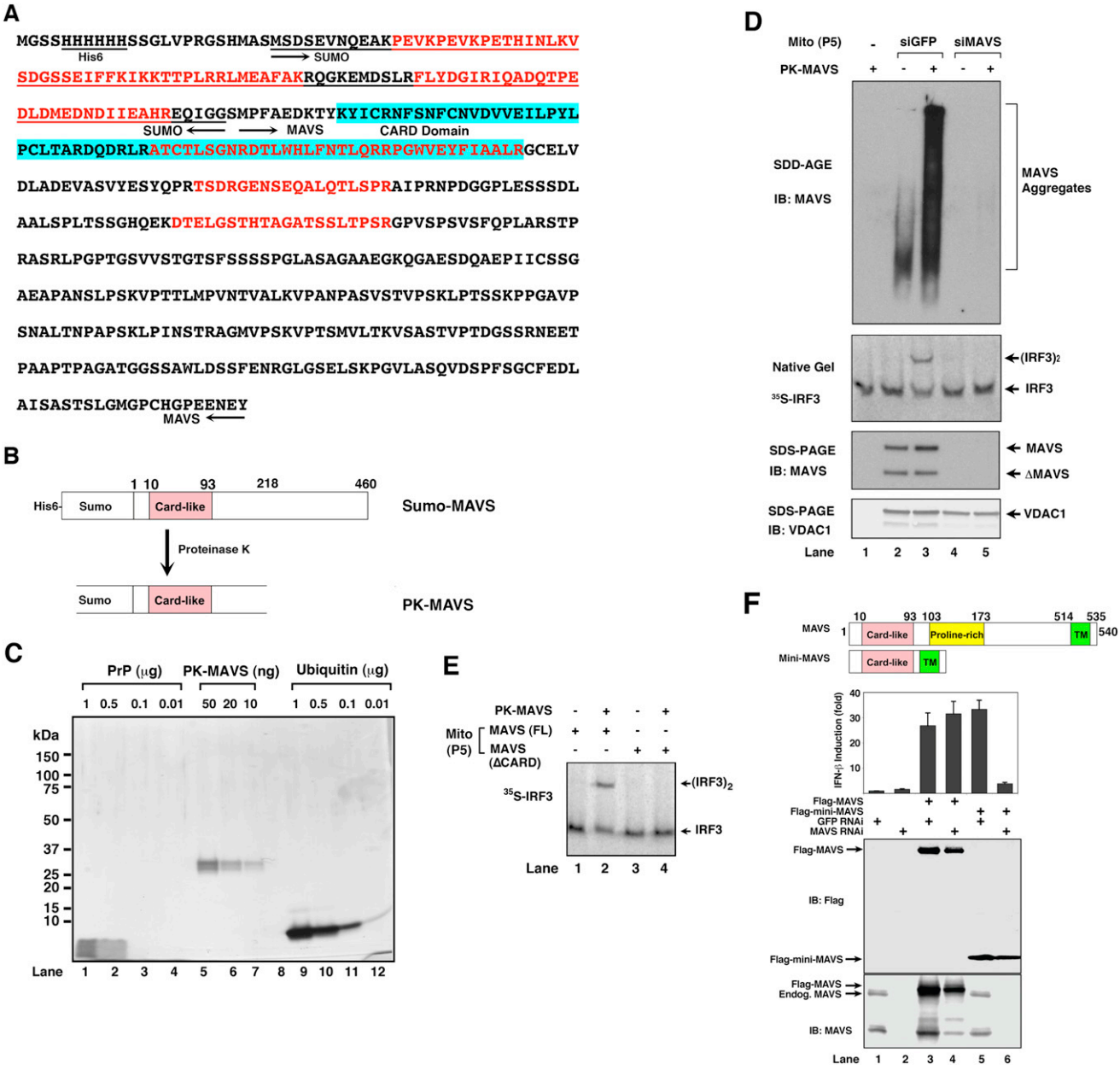

Figure S4. Characterization of Proteinase K-Resistant MAVS and Mini-MAVS, Related to Figure 4

(A) Sequencing of PK-MAVS by tandem mass spectrometry (MS/MS). The sequence of His_6-Sumo-MAVS, which lacks the proline-rich region (103-153) and C terminus (461-540), is shown. Peptides identified by MS/MS are shown in red, the MAVS CARD domain is in cyan, and the Sumo sequence is underlined. The beginning and end of Sumo and MAVS sequences are depicted as arrows.

(B) Diagram depicting Sumo-MAVS and PK-MAVS before and after proteinase K digestion.

(C) Silver staining of different amounts of PrP, PK-MAVS and ubiquitin.

(D) Mitochondria isolated from HEK293T cells transfected with siRNA against MAVS or GFP (control) were incubated with PK-MAVS for 10 min. Aliquots of the mitochondria were assayed for MAVS aggregation and activity. Mitochondrial extracts were immunoblotted with antibodies against MAVS or VDAC1.

(E) *Mavs*$^{-/-}$ MEF cells reconstituted with full-length MAVS or MAVSΔCARD were used to isolate mitochondria, which were then incubated with PK-MAVS for 10 min. The activity of MAVS in the mitochondria was measured by IRF3 dimerization assay.

(F) Mini-MAVS requires endogenous MAVS to induce IFN-β. HEK293T-IFNβ-Luciferase reporter cells were transfected with siRNA against GFP (as a control) or MAVS two days before transfection with Flag-tagged expression vectors for MAVS or mini-MAVS, both of which were resistant to the MAVS siRNA. Cell lysates were prepared for luciferase assay or immunoblotting with the indicated antibodies.

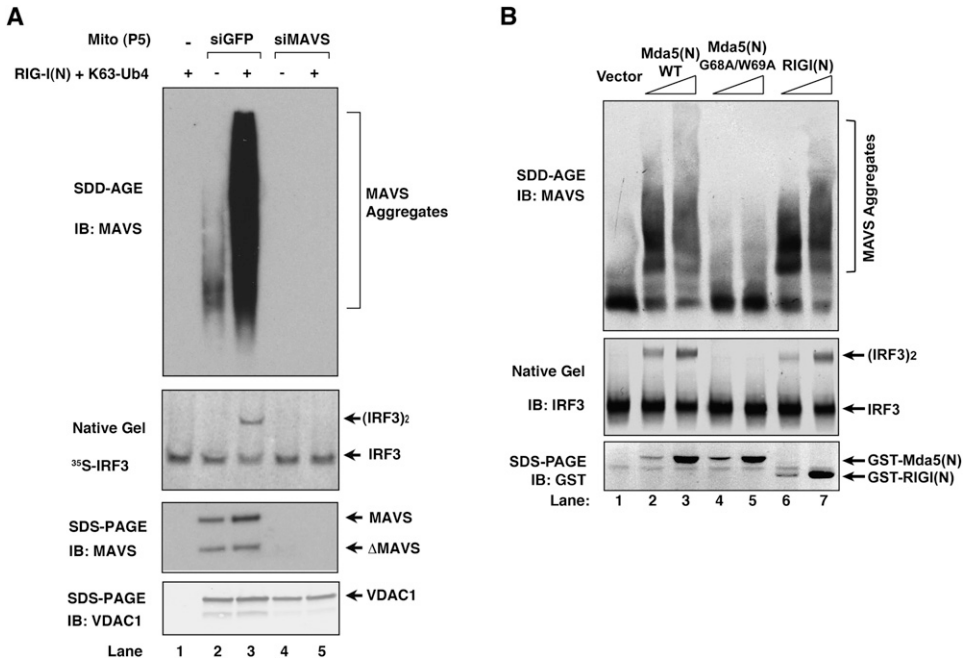

Figure S5. Both RIG-I and MDA5 Induce MAVS Aggregation, Related to Figure 6

(A) Mitochondria (P5) were isolated from HEK293T cells transfected with siRNA against MAVS or GFP (control), and incubated with RIG-I(N) and K63-Ub4 for 10 min. MAVS aggregation and activity in the mitochondria were measured by SDD-AGE and IRF3 dimerization assays, respectively. Aliquots of the mitochondrial extracts were immunoblotted with an antibody against MAVS or VDAC1.

(B) Expression vectors encoding GST-tagged RIG-I(N), MDA5(N) or MDA5(N)-G68A/W69A were transfected into HEK293T cells. 24 hr later, the mitochondria from the transfected cells were isolated to measure MAVS aggregation by SDD-AGE. IRF3 dimerization and the GST-tagged proteins in the cytosol were analyzed by immunoblotting following native gel electrophoresis and SDS-PAGE, respectively.